TEKTONIKA

A Snapshot of the Earliest Stages of Normal Fault Growth

Ahmed Alghuraybi *[1], **Rebecca Bell** [1], **Christopher A. Jackson** [1]

[1]Landscapes and Basins Research Group (LBRG), Department of Earth Science and Engineering, Imperial College London, London, UK

Abstract Observations of how faults lengthen and accrue displacement during the very earliest stages of their growth are limited, reflecting the fact that the early syn-kinematic sediments that record this growth are often deeply buried and difficult to image with geophysical data. Here, we use borehole and high-quality 3D seismic reflection data from SW Barents Sea, offshore Norway to quantify the lateral propagation (c. 0.38–3.4 mm/year) and displacement accumulation (c. 0.0062–0.025 mm/year) rates (averaged over 6.2 Myr) for several long (up to 43 km), moderate displacement (up to 155 m), syn-kinematic faults that we argue provide a unique, essentially 'fossilised' snapshot of the earliest stage of fault growth. We show that lateral propagation rates were up to 300 times faster than displacement rates during the initial ~25% of fault lifespan, suggesting that these faults lengthened much more rapidly than they accrued displacement. Our inference of rapid lengthening is also supported by geometric observations including: (i) low D_{max}/L_{max} (<0.01) scaling relationships, ii) high (>5) length/height aspect ratios, iii) broad, bell-shaped throw-length profiles, and iv) hangingwall depocenters forming during deposition of the first seismically detectable stratigraphic unit spanning the length of the fault. We suggest that the high ratio between lateral propagation rate and displacement rate is likely due to relative immaturity of the studied fault system, an interpretation that supports the 'constant-length' fault growth model. Our results highlight the need to document both displacement and lateral propagation rates to further our understanding of how faults evolve across various temporal and spatial scales.

Executive Editor: **Gwenn Péron-Pinvidic**
Associate Editor: **Frank Zwaan**
Technical Editor: **Mohamed Gouiza**

Reviewers: **Lisa McNeill**, **Vincent Roche**

Submitted: **6 December 2022**
Accepted: **3 July 2023**
Published: **27 July 2023**

1 Introduction

Normal faults are an expression of extensional strain in the Earth's crust. They define the physiography of rifted landscapes and seascapes, and control the distribution and production of important energy resources (e.g., geothermal, hydrocarbon), and the location and safety of storage sites for hazardous waste (e.g., nuclear, CO_2). Normal faults are also associated with hazardous earthquakes that threaten lives, livelihoods, and critical infrastructure. Documenting the rates at which normal faults slip and grow is thus critical to understanding the timescales over which landscapes develop and, in turn, how variable slip and lateral tip propagation rates, and fault geometry more generally, impacts sediment dispersal and the distribution of sedimentary facies. Fault geometry and related host rock strain also influence subsurface fluid flow and accumulation by controlling fault architecture and fault zone properties, such as permeability. There are currently two end-member fault growth models: (i) the 'propagating fault model' and (ii) the 'constant length model'. The former arises from the apparent scaling relationship between maximum fault displacement (D_{max}) and length (L_{max}) and proposes that faults grow by simultaneously accumulating length and displacement (where D_{max}/L_{max} typically ranges between 1–0.01; e.g., *Watterson*, 1986; *Walsh and Watterson*, 1988; *Cowie and Scholz*, 1992; *Schlische et al.*, 1996; *Walsh et al.*, 2003). However, global D_{max}-L_{max} datasets show a high degree of scatter (e.g., *Rotevatn et al.*, 2019), which may reflect, for example, differences in the geological setting within which the studied fault network formed, or uncertainties in measuring the key geometric parameters due to seismic imaging quality or outcrop extent (e.g., *Walsh and Watterson*, 1988; *Gillespie et al.*, 1992; *Kim and Sanderson*, 2005). An alternative interpretation is that this variability results from fault maturity, related to the fact that some faults may attain their near-final lengths before accumulating significant displacement (i.e., the latter, constant-length fault model; e.g., *Walsh et al.*, 2002; *Meyer et al.*, 2002; *Nicol et al.*, 2005, 2016; *Childs et al.*, 2017; *Rotevatn et al.*, 2019; *Nicol et al.*, 2020; *Lathrop et al.*, 2022). Different definitions of fault maturity exist in the literature. For example, *Manighetti et al.* (2007) defines fault maturity based on a combination of four criteria (trace length ≥ 1000km and/or Initiation Age ≥ 10Ma and/or Slip Rate c. few cm/yr and/or Total Displacement ≥ 100km. In contrast, other studies focused on normal fault growth characterised mature fault systems as those that experienced multiple phases of change in their lengths and location of fault activity (*Morley*, 1999), while immature fault systems as hav-

*✉ a.alghuraybi19@imperial.ac.uk

ing many relatively short <4km interacting fault traces (e.g., *Nicol et al.*, 2010). However, we classify in this paper that an immature normal fault as being one that is still on its trajectory of increasing in length with minimal displacement (i.e., rapid tip propagation and segment linkage) and a mature fault is where its displacement increases with a little increase in fault length (i.e., dominant displacement accrual and constant length) (modified after *Rotevatn et al.*, 2019). The rate of fault slip determines the recurrence interval of potentially hazardous earthquakes, meaning an improved understanding of seismic hazard can be gained by studying slip rate and fault growth of both ancient (i.e., inactive) and active faults.

Regardless of the precise mode of growth, previous studies have shown that strong mechanical anisotropy in the faulted, horizontally layered host rock can restrict the vertical propagation of faults (e.g., *Nicol et al.*, 1996; *Soliva and Benedicto*, 2005; *Roche et al.*, 2013) (*Schultz and Fossen*, 2002). Faults forming in these rocks may have anomalously high fault aspect ratios (i.e., fault's length to height ratio of 3–13, compared to 1–3 for more typical faults) and strikingly low D/L scaling relationships (i.e., $D_{max}/L < 0.01$) (e.g., *Nicol et al.*, 1996; *Schlische et al.*, 1996; *Schultz and Fossen*, 2002; *Soliva and Benedicto*, 2005; *Roche et al.*, 2013).

The rate at which faults lengthen and accumulate displacement is a key element of their kinematic history and influences the role they play in controlling the geomorphology, seismic hazard, and resource potential of rift basins (e.g., *Walsh et al.*, 2003). Depending on the period and type of observation, displacement rates vary. For example, over relatively short observational periods (10s years), GPS/geodetic data show that displacement rates can be relatively fast (>10 mm yr^{-1}) and highly variable (e.g., *Briole et al.*, 2000; *Wallace et al.*, 2014) compared to longer-period, typically more stable geological displacement rates (<1 mm yr^{-1}) derived from seismic reflection or field data (e.g. *Mouslopoulou et al.*, 2009; *Cowie et al.*, 2012; *Mouslopoulou et al.*, 2012). This may relate to earthquake clustering events, enhancing modern displacement rate estimates over short observational periods (e.g., *Cowie et al.*, 1993; *Friedrich et al.*, 2003; *Robinson et al.*, 2009).

In contrast to displacement, lateral fault tip propagation rates are less frequently reported in fault growth studies, especially over short observational periods. The reason for this varies based on the type of study and dataset used. For example, GPS data can provide some measure of coseismic fault throw (i.e., the vertical component of displacement field derived from GPS location and elevation records) and interseismic creep, but not typically lateral propagation (e.g., *Blakeslee and Kattenhorn*, 2013). Field studies tend to rely on geomorphic analysis of near-tip drainage patterns (e.g., *Jackson et al.*, 1996) and marine terraces (e.g., *Morewood and Roberts*, 1999), or the stratigraphic architecture of syn-rift strata (e.g., *Gawthorpe et al.*, 1997) to infer lateral propagation rates, although these methods are limited in that they demand well-preserved exposures. These studies show that lateral fault propagation rates can be considerably faster than throw rates (e.g., *Morewood and Roberts*, 1999). However, our current understanding of fault growth, in particular how fluctuations in displacement and lateral propagation rate relate to changes in fault geometry (i.e., aspect ratio), remains poorly constrained. More generally, fault growth models need to quantify both lateral propagation and displacement rates such that they exist within a temporal framework and can thus provide the structural foundation for the tectono-stratigraphic analysis of rift basins at a range of scales (e.g., *Walsh et al.*, 2002; *Rotevatn et al.*, 2019).

Constraining the patterns and rates of fault growth requires the analysis of age-constrained syn-kinematic strata (i.e., strata deposited whilst the fault is active) along the length of faults in three dimensions (3D). High-quality 3D seismic reflection data with accompanying biostratigraphy from wells is generally only available from ancient (i.e., inactive), hydrocarbon-bearing rift basins where the syn-rift growth packages are deeply buried and poorly seismically resolved. Alternatively, in active rifts where the syn-rift sediments are shallower (but there is no/limited hydrocarbon interest), the available seismic reflection data are only 2D and often lack age constraints on the syn-rift strata, which could explain the limited observations on the earliest stages of normal fault growth. For example, Lake Malawi and Lake Tanganyika in the East African Rift system contain > 5km of syn-rift sediments each (e.g., *Scholz et al.*, 1998). These syn-rift deposits enable the study of intra- and early-rift processes (e.g., *Shillington et al.*, 2020). However, these deposits are covered by only 2D seismic reflection profiles and lack the necessary age constraints needed for a detailed analysis of the earliest stages of normal fault growth. Similarly, in the Icelandic Rift Zone, data from Thingvallavatn were used to study the fault and magmatic interaction over a 9 kyr period (*Bull et al.*, 2003). However, due to the relatively limited data quality (single-fold seismic) and reliance on a single age constraint (provided by dating a lava flow), the kinematic analysis of normal fault growth was rather limited. In other active rifts like the Red Sea or Gulf of Suez, where the syn-rift deposits are exposed, the stratigraphic architecture of syn-rift strata (e.g., *Gawthorpe et al.*, 1997) can be used to infer lateral propagation rates. However, such studies are often limited in that they demand areally extensive, high-quality exposures of dateable material.

We here use age-constrained, high-quality 3D seismic reflection and borehole data from the SW Barents Sea to determine the lateral propagation and displacement rates for several ancient basal tip-restricted syn-kinematic faults (i.e., faults that are bound by a base mudstone layer that inhibits downward propagation whereas their upward propagation is restricted by the free-surface) that we suggest were

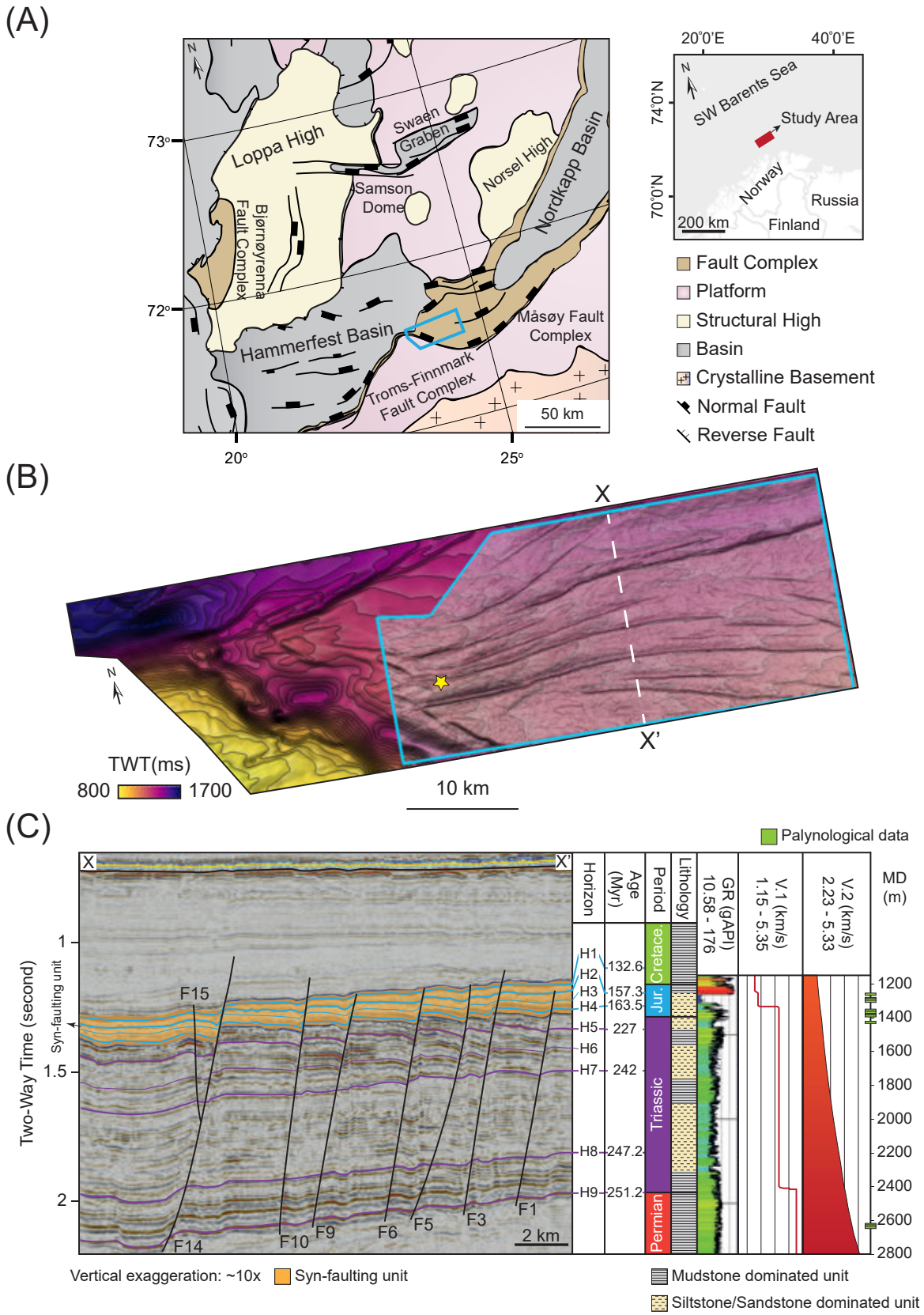

Figure 1 – **(A)** Map showing study area location and regional geology of SW Barents Sea. The map is modified after information found in the Norwegian Petroleum Directorate fact page http://www.npd.no/en/. **(B)** A time-structure map of the base syn-kinematic unit (H4) with a white-dashed line indicating the location of the seismic section in (C). The location of wellbore 7124/4-1S is noted by a yellow star while the study area is outlined by the blue border. **(C)** A representative seismic cross-section highlighting the geometry of the studied faults and horizon's age and lithology as constrained by wellbore 7124/4-1S. The section also includes Gamma Ray (GR) log data, modelled interval velocity using simplified geological model (V.1) and calculated pseudo interval velocity using estimated time-depth relationship from seismic well tie (V.2).

abandoned before reaching fault maturity. These are exceptionally well characterised faults, thus provide a snapshot of the earliest stage of fault growth rarely seen in active rifts due to lack of comparable 3D spatial and temporal data coverage.

2 Geological Setting

We have studied a system of low-displacement (< 150m throw), Middle Jurassic-to-Early Cretaceous normal faults in the SW Barents Sea offshore northern Norway (Figure 1). The SW Barents Sea is a present-day passive margin that experienced multiple phases of rifting that started following the collapse of the Caledonian orogenic belt in the Devonian and ended in the Eocene with the opening of the Norwegian and Greenland seas and initiation of seafloor spreading (e.g., *Faleide et al.*, 2008). These rift phases helped shaped the large-scale structure of the region (i.e., NNE-trending rift basins like the Hammerfest, Nordkapp and Sørvestsnaget basins, and basement highs like the Loppa, Stappen and Fedynsky highs; Figure 1A) and included the rift phase in the Middle Jurassic to Early Cretaceous that formed the faults studied here (e.g., *Faleide et al.*, 2008). Three lines of evidence suggest that the studied fault system is tectonic (i.e., formed via upper crustal extension imposed by far-field stresses) rather than gravitational (i.e., formed by relatively local extension above a tilted, ductile intra-stratal detachment). First, the faults strike perpendicular to the NNW-SSE extension direction associated with Middle Jurassic to Early Cretaceous rifting. Second, in a gravity-driven deformation setting, one would expect the basal detachment to be tilted in the direction of fault dip and for these faults to be listric (e.g., *Spathopoulos*, 1996; *Corredor et al.*, 2005; *Robson et al.*, 2017), neither of which are the case here. Finally, extension within gravity-driven systems is typically associated with complimentary shortening in the form of folding and thrusting; again, this is not observed within the study area. The faults developed in Upper Permian/-Triassic to Lower Cretaceous clastic rocks deposited on Caledonian crystalline basement (e.g., *Doré*, 1995). The faulted host rock is characterised by strong mechanical competency contrast between alternating intervals of relatively weak, mudstone-rich strata (i.e., Upper Permian) and mechanically stronger, siltstone- and sandstone-rich layers (i.e., Triassic) (see lithology column in Fig. 1C; see also the formation evaluation and gamma-ray log, and lithology well-log in wellbore 7124/4-1S (*NPD*, 2023)).

3 Data and Method

We use pre-stack time-migrated 3D seismic reflection data covering c. 533 km2 and with an estimated vertical resolution of 12.5–25 m in the depth range of interest (see Figure SI-1, in Supporting Information). The survey has an approximate visibility (or detectability) limit of c. 5 m (see *Osagiede et al.*, 2014, and references therein). These data allow us to map and describe the map-view and cross-sectional geometry of the studied fault network, and by collecting throw data for nine horizons (seven are age-constrained by well data and two of unknown age that mark distinct changes in seismic facies) to show how throw varies across the fault surfaces (Figure 11). The horizons' ages were constrained by palynological data from wellbore 7124/4-1S (Figure 1B and C; see also Table SI-1, in Supporting Information, for palynological data sample spacing and depth). Two of the age-constrained horizons (H1 and H4) mark the top and base of the syn-faulting strata, with one occurring within the middle of this unit (see highlighted seismic section in Figure 1C). The age difference between the top and base syn-faulting horizons, therefore, dates the total duration of fault activity.

We provide detailed descriptions of our methods in Figure 2. First, we measure throw values at a 250 m interval on seismic lines trending perpendicular to fault strike and analyse throw values using throw-length (T-x) and throw-depth (T-z) plots (Figure 2; e.g., *Cartwright et al.*, 1995; *Jackson et al.*, 2017). We also produce isochron (time-thickness) maps (to analyse spatial and temporal trends in across-fault thickening; see *Schlische et al.*, 1996; *Gawthorpe et al.*, 2003; *Jackson and Rotevatn*, 2013), throw strike-projections (a plot of throw values across a fault surface; Figure 2E; also see *Walsh and Watterson*, 1991; *Alghuraybi et al.*, 2022), and expansion index (EI) analysis (dividing hangingwall thickness by footwall thickness for corresponding stratal units to constrain the initiation, variability, and cessation of fault activity (Figure 2B); see *Cartwright et al.*, 1998; *Jackson and Rotevatn*, 2013) to further describe the geometry of the fault network and critically assess associated variations in the thickness of syn-kinematic strata (see review by *Walsh and Watterson*, 1991; *Jackson et al.*, 2017). We also examine fault growth through time by performing throw backstripping, a technique that involves successively subtracting the throw accumulated on shallower, younger horizons from deeper, older ones (see review by *Jackson et al.*, 2017). All seismic sections are displayed with SEG European Convention (*Brown*, 2001) with a downward increase and decrease in acoustic impedance represented by a peak (red) and a trough (blue), respectively. Note that all the seismic and wellbore data can be accessed from the Diskos NDR (https://portal.diskos.cgg.com/whereoil-data/) by searching for "Fruholmen 3D" and the well data can be found by searching for "7124/4-1 S". We use velocities derived directly from average sonic log responses from the wellbore that correspond with key seismic intervals (V1; Figure 1C) to create a time-depth relationship. We then apply the generated time-depth relationship to perform our seismic-well-tie (V.2; Figure 1C) and convert our time measurements from ms TWT (milliseconds two-way time) to depth (Figure 1C). The uncertainty in throw arising from using our depth-conversion approach is ±12%; this value arises by comparing the range of velocities

(A) Cross-section

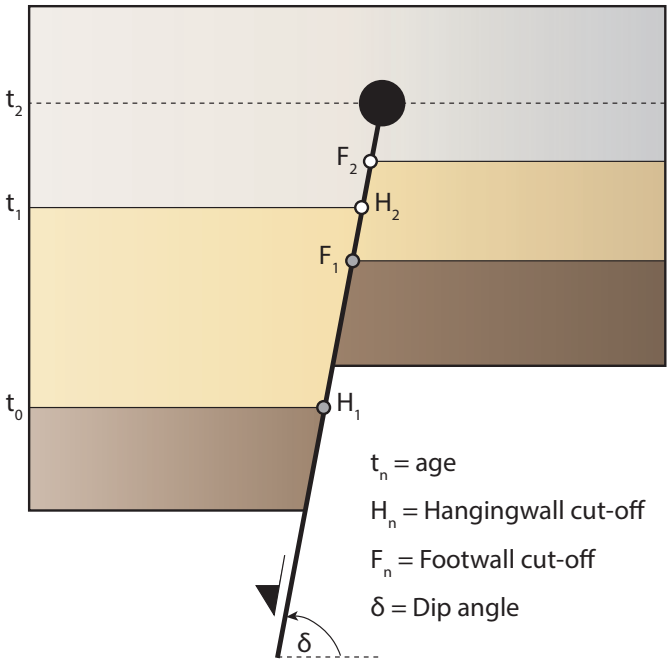

(B) Calculations

$$Throw_n = H_n - F_n$$

$$Displacement_n = \frac{H_n - F_n}{Sin\delta}$$

$$Displacement\ Rate_{t0\text{-}t1} = \frac{Displacement_1 - Displacement_2}{t_0 - t_1}$$

$$Displacement\ Rate_{t1\text{-}t2} = \frac{Displacement_2}{t_1 - t_2}$$

$$Half\ Length_1 = x_1 - x_0 \ ; \ Half\ Length_2 = x_2 - x_1$$

$$Lateral\ Propagation\ Rate_1 = \frac{Half\ Length_1}{t_0 - t_1}$$

$$Lateral\ Propagation\ Rate_2 = \frac{Half\ Length_2}{t_1 - t_2}$$

$$Aspect\ Ratio = \frac{Length}{Height} \quad ; \quad Expansion\ Index_n = \frac{H_n - H_{n+1}}{F_n - F_{n+1}}$$

(C) Map-view

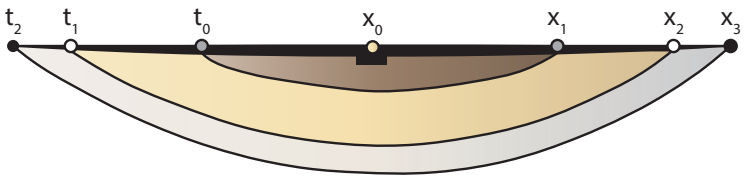

(D) Displacement-length profile

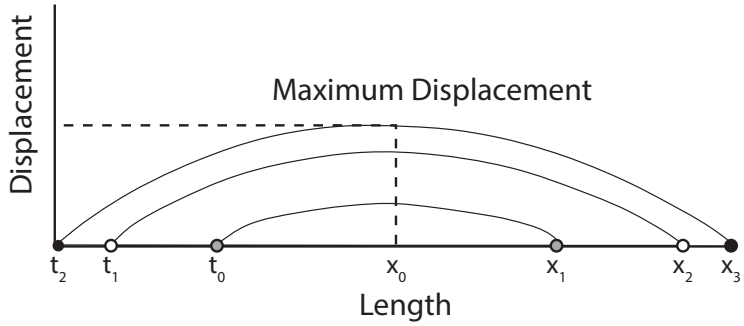

(E) Strike-projection

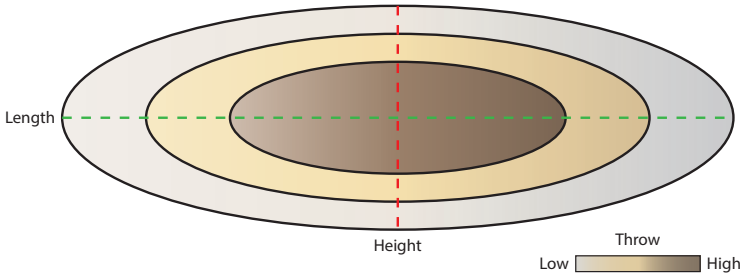

Figure 2 – Detailed description of the methodology we use to calculate fault throw, displacement, displacement accumulation rate (Displacement Rate), lateral propagation rate (Lateral Propagation Rate), fault length / height aspect ratio (Aspect Ratio), and expansion index (EI).

we obtain for the Jurassic interval with regional velocity modelling and regional wellbore data presented by others (e.g., *Clark et al.*, 2013; *Rojo et al.*, 2019) (see Appendix 1 in *Alghuraybi*, 2023).

We estimate the lateral fault tip propagation rate by taking the fault half-length as measured at the base of the syn-kinematic interval (H4) and dividing it by the time interval to the next age-constrained unit that shows across-fault thickening (i.e., we establish the duration and length of major depocenter development and calculate the lateral bi-directional propagation rate of the fault tips (Figure 2); cf. *Childs et al.*, 2003). Similarly, we calculate the displacement rate by dividing the backstripped displacement (i.e., displacement for the time interval) by the time interval to the next age-constrained horizon (e.g., *Nicol et al.*, 1997; *Bell et al.*, 2009). The displacement value is calculated using measured throw multiplied by fault dip angle (i.e., the inclination of a fault plane relative to a horizontal plane). The fault dip estimation contributes to an added uncertainty that should be considered. We calculate displacement rate at every along-strike location where we made a complimentary throw measurement (i.e., at 250 m intervals for a total of c. 1100 measurement point). Then, we take the minimum and maximum displacement rates for each fault to capture their full range of behaviour. This results in two displacement rate measurements for each of the 15 studied faults. We then compare these slip rates (lateral propagation and displacement rates) with data from 29 other global datasets from normal faults that formed (or are forming in still-active settings) in various tectonic and depositional settings (see Figure SI-2, in Supporting Information, and Appendix 2, in *Alghuraybi*, 2023, for a full list of references).

We calculate the displacement and lateral propagation rates using the time between the two dated horizons at the base (H4) and middle (H2) of the syn-kinematic package (Fig. 1C; sequence with best palynological age control). This results in a period of 6.2 Myrs, which we argue should be considered as an upper limit of the duration of what we refer to as early-stage fault activity. In fact, our detailed geometric analysis showed that the strike-parallel depocenters formed in the hangingwalls of the studied faults over a shorter period than the time between the two horizons defining the top and middle of the syn-kinematic package (<6.2 Myr), however we do not have age-control on horizons between H4 and H2. In the absence of higher resolution age constraints, we speculate that the similarity in seismic facies characteristics throughout the syn-kinematic interval indicates that the: (i) lithology; (ii) depositional style; and (ii) sediment accumulation rate did not vary significantly during the syn-kinematic period (c. 7 m/Myr for the 6.2 Myr period, based on wellbore data). If the sediment accumulation rate was constant, then we might infer the duration of the earliest stage of fault development (i.e., the time duration between horizon H4 and H3) to be c. 3.1 Myrs instead of 6.2 Myr, based on the observation that the thickness of the earliest seismically resolvable depocenter is c. 50% of the total thickness of the 6.2 Myr syn-kinematic package (Figures 1C, 8, and 9A). Therefore, the values we show should be regarded as lower estimates of displacement and lateral propagation rates of the studied fault network, given we show rates calculated using a duration of 6.2 Myr. Additional borehole-derived age data, derived from the hangingwall fill of one or more faults, would help further refine our calculations.

4 Results

4.1 Fault Network Geometry

We mapped a total of 87 faults, including some secondary faults (synthetic and antithetic), oblique faults, and the major, basin-bounding faults (i.e., the TFFC, which is located in the SW of the study area; see *Alghuraybi et al.*, 2022, for more details on the fault networks in the area). However, we decided to focus on the 15 largest E-W-striking faults within the network, given they are particularly well-imaged in our seismic data, thus allowing us to undertake a detailed kinematic analysis. The studied fault network consists of 15 Middle Jurassic to Early Cretaceous faults, offsetting Early Triassic to Early Cretaceous stratigraphy (Figures 1B, 1C, and 3A). Most of these faults tip-out downwards in mudstone-dominated, Permian strata, die-out upwards into Early Cretaceous strata, and are associated with Upper Jurassic growth strata (i.e., they were active in the Middle Jurassic – Early Cretaceous; Fig. 3BA). Critically, other stratal units are offset by but do not thicken across the faults, although they thicken regionally, towards the NW, towards the Atlantic margin (Figure 3B–D). The studied faults are not associated with clear fault bends, abandoned splays or relays (Figure 3A). Most faults are also unusual in that they are: i) notably underdisplaced with respect to their lengths (D_{max}/L_{max} = c. 0.001; Figure 4A); and ii) have anomalously high (up to 25) aspect ratios (Figure 4B). Despite having a broad, bell-shaped throw-length profile at the base syn-kinematic level (H4) (Figure 4C), the fault network shows variable throw-depth profiles with no clear trend representative of all the faults within the network (Figure 4D.i). However, in detail, we can identify two broad subsets of faults: (a) Subset 1, with throw maxima located at the base of the syn-kinematic interval (H4) and decreasing throw values with depth (Figure 4D.ii); and (b) subset 2, which is characterised by two maximum throw values, located at H4 and H9, that are separated by a throw minimum located at H7 (Figure 4D.iii). Some of the studied faults are tip-restricted (e.g., F2, F6, F8, F9, F10, F13) as they intersect oblique faults. There is undoubted uncertainty in constraining fault lengths for faults that likely extend outside of the seismic survey (e.g., F1, F3, F4, F6, F14). However, by incorporating other observations (such as throw measurements and throw-length profiles), we argue that in the case of faults F1, F3, and F6, throw approaches zero near the edge of the seis-

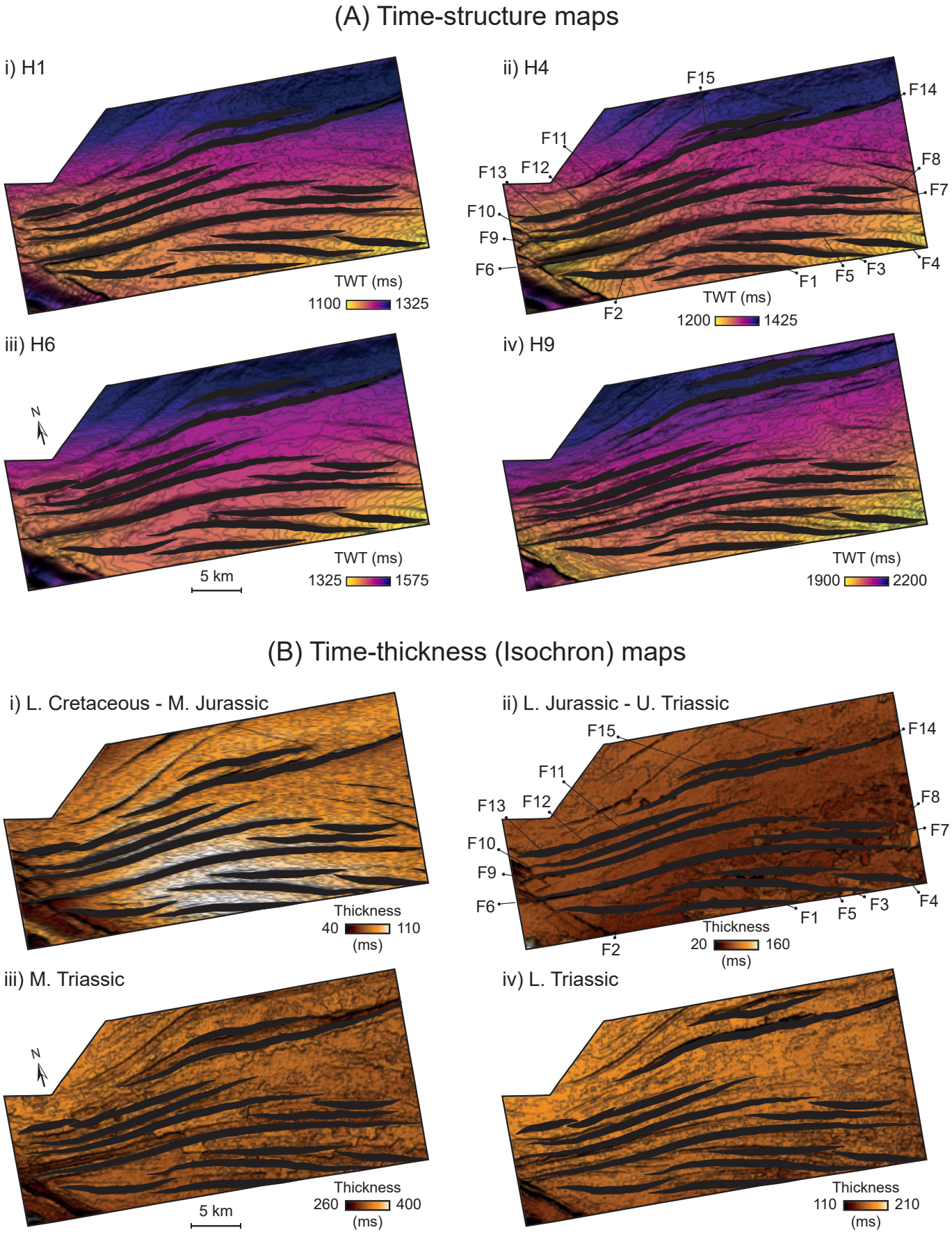

Figure 3 – **(A)** Time-structure maps for the Early Cretaceous - H1 **(A.i)**, Middle Jurassic - H4 **(A.ii)**, Middle Triassic - H6 **(A.iii)** and Lower Triassic/Upper Permian - H9 **(A.iv)** horizons. The location of the fault network and names of the studied faults are annotated on (A.ii). **(B)** Isochron (time-thickness) maps for the L. Cretaceous to M. Jurassic **(B.i)**, L. Jurassic to U. Triassic **(B.ii)**, M. Triassic **(B.iii)** and L. Triassic **(B.iv)**. These isochrons show the clear across-fault thickening in the Early Cretaceous to Middle Jurassic and general constant thickness nature of the other time intervals.

mic survey. Therefore, based on the broad bell-curve shape of the throw-length profile and the decreasing throw values, we suggest that the fault tip lies a short distance outside of the survey, and that the observed length is only a little less than the overall fault length. Here, we present a detailed geometric analysis of six faults (three from subset 1 (Faults 1, 6 and 8) and three from subset 2 (Faults 5, 9 and 14), which are representative of the range of geometric characteristics observed within the fault network.

4.1.1 Observations

Fault 1 (F1; Fig. 5A) is approximately 15 km long, with a maximum throw of c. 22 ms (c. 32 m; see depth conversion in Fig. Figure 1C) and a maximum displacement of c. 42 m. The longest fault in the network is Fault 6 (F6; Figure 5B), which is c. 43 km long, and that has a maximum throw of c. 72 ms (c. 110 m) and a maximum displacement of c. 130 m. Similar to F1 and F6, Fault 8 (F8) strikes E-W, dips to the N and appears to have throw maxima at the base of the syn-kinematic interval (i.e., base Upper Jurassic; Figures 5A, 5B, and 6A). F8 is c. 10 km long and has a maximum throw and displacement of c. 34 ms (c. 50 m) and c. 66 m, respectively. Faults 1, 6, and 8 are part of subset 1 of the studied fault network and have aspect ratios of c. 13, 25, and 10 (Figure 4B, D.ii).

The remaining three faults (Faults 5, 9, and 14) are part of subset 2 (Figure 4D.iii). Like those in subset 1, these faults strike E-W and dip to the N. Fault 5 (F5; Figure 6B) is c. 15 km long and has a maximum throw of c. 33 ms (c. 50 m) and a maximum displacement of c. 71 m. In contrast, Fault 9 (F9; Figure 7A) is almost twice as long as F5 (c. 31 km long) and has comparable maximum throw and displacement values of c. 55 ms (c. 83 m) and c. 104 m. Like F9, Fault 14 (F14) is also c. 31 km long (Figure 7B). However, F14 has nearly twice as much maximum throw and displacement as F9 (Figure 7B). Both F9 and F14 have aspect ratios of c. 19, whereas F5 has an aspect ratio of c. 11 (Figure 4B).

The Upper Jurassic strata thicken across all faults within the studied network with EI values >1 for all faults (up to 2.2 and 1.7 for F6 and F9 respectively), defining strike-parallel and elongate depocenters (Figure 3B, A). We make two key observations here regarding the fault network. The first is that the lowermost reflections in the Upper Jurassic package onlap onto the base syn-kinematic horizon immediately adjacent to the fault tips (H4) (Figure 8). Although this onlapping relationship is easier to see adjacent to faults associated with thicker Upper Jurassic growth stratigraphy (e.g., F6; Fig. 8C, D), it can also be assumed for other faults where the thickness between the lowermost Upper Jurassic package reflections and the base syn-kinematic horizon (H4) is sufficiently small that it is approaching the seismic tuning thickness for our data (c. 14 – 18 m at H4 level). In these cases, instead of the reflections onlapping and truncating in the middle of the fault as they appear in the seismic data, the reflections are likely thinning and onlapping onto H4 closer to the fault tip (Figure 8A, B). In some of our subsurface examples, the relatively limited spatial resolution of our seismic reflection dataset limits our ability to interpret the detailed stratigraphic termination and onlap styles readily identified in the field (i.e., we observe only reflection thinning and tuning, and not discrete onlap; e.g., *Bakke et al.*, 2013). The second key observation is that Upper Jurassic growth strata clearly thicken across the faults just inboard of their fault tips (Figure 9A). In fact, we observe the development of strike-parallel depocenters and their associated across-fault thickening of growth strata in the lowermost seismically resolvable unit (H3-H4) (Figure 9A.i). For instance, we can see that the location of the fault tips and formation of the strike-parallel depocenters are corresponding with the base syn-kinematic horizon having EI values of >1 and the highest backstripped throw along-strike of both F6 and F9 (Figure 9A.v–viii).

4.1.2 Interpretation

Growth strata show that the studied faults were active from 163.5–132.6 Ma (i.e., in the Middle Jurassic–Early Cretaceous (H4-H1); Figures 3B.i, 7B) for both subsets 1 and 2. The presence of multiple throw maxima along the same stratigraphic level on some of the subset 1 faults (e.g., F1 and F6; Figure 5A, B) may provide geometric evidence that they grew by lateral segment linkage (e.g., *Cartwright et al.*, 1995). However, the lack of obvious bends, breached relays, or abandoned splays suggests that the precursor segments did not overlap, and may have formed as part of a single, kinematically linked structure from their inception (e.g. *Childs et al.*, 2017). Instead, these throw maxima might relate to across-strike throw partitioning between adjacent faults. For example, where F6 decreases in throw towards its eastern tip, throw on the adjacent F7 increases near its western tip (Figures 3A.ii, 5B). The interpretation that geometrically segmented faults formed part of a kinematically coherent system from their inception is supported by the fact that the across-fault thickening we observe occurs along almost the entire strike-length of the faults and is associated with onlap of the lowermost syn-kinematic onto pre-kinematic strata immediately inboard of the lateral fault tips (Figure 8). In contrast, based on the observation that subset 2 faults have multiple throw maxima along different stratigraphic intervals (H4, H9) that are separated by a throw minimum that occurs at the same stratigraphic interval for all faults (H7), we suggest the presence of an intraformational detachment layer in addition to the lower, regional detachment onto which all faults terminate (Figure 4D). By analysing the map-view locations of where vertical linkage occurred, we do not see any strong trends that highlight areas of favourable vertical linkage (Figure 9B). Instead, the lack of any clear trends suggests that the strong mechanical anisotropy observed from the wellbore data

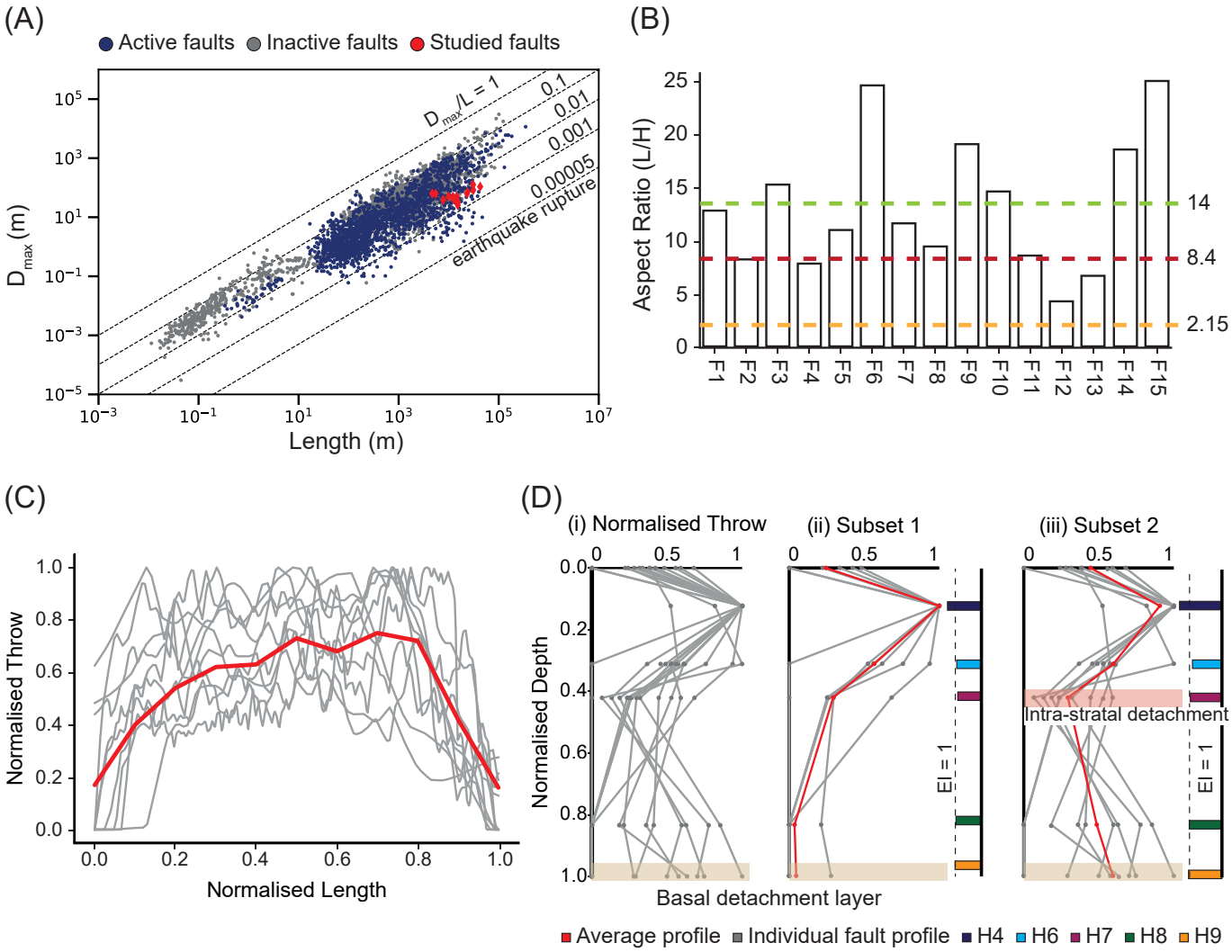

Figure 4 – A summary of the geometric properties of the fault network showing **(A)** D_{max}/L_{max} plot from a global database of normal faults (modified after *Lathrop et al.*, 2022). Data for studied fault network are shown in red while literature data are showing in blue (active faults) and grey (inactive faults). **(B)** Aspect ratio (length/height) distribution of the studied fault network with dashed-horizontal lines showing average aspect ratios of "blind isolated normal faults in layered sequences" (yellow), maximum aspect ratio of restricted faults (red) (*Nicol et al.*, 1996) and maximum aspect ratio for faults cutting formations with strong mechanical contrast (green) (*Roche et al.*, 2021). **(C)** Normalised throw-length plot for the studied faults (grey) at the base syn-kinematic level (H4) with an average profile of the fault network shown in red. **(D)** Normalised throw-depth profiles for the studied faults showing the basal detachment layer **(i)**. The fault network can be divided into two subsets with subset 1 including faults F1, F4, F6, F8, F13 and F11 **(ii)** showing a single throw maximum at the H4 level while subset 2 (F2, F3, F5, F7, F9, F10, F11, F12, and F14) **(iii)** shows the presence of a potential intra-stratal detachment layer that separates two throw maxima denoting potential vertical (i.e., dip) linkage. The Expansion Index (EI) values of H4, H6, H7, H8 and H9 are shown to the side of the normalised throw-depth plots.

(Figure 1C) might also vary laterally across the study area.

4.2 Fault Growth Rates

In addition to the geometric properties of the fault network, we also assess the kinematics of its constituent faults, with a specific focus on their displacement and lateral propagation rates. We then compare and contextualise these with rates derived from 29 other locations (Figure 10A). Spanning various tectonic and depositional settings, and derived from active and inactive faults, our compiled dataset is not intended to be exhaustive; it simply allows us to compare our faults with some global examples of rates determined across different observational periods.

Our studied faults show relatively low displacement rates compared to the global dataset (i.e., c. 0.0062–0.025 mm/year averaged over a 6.2 Myr period of fault activity and c. 0.012–0.050 mm/year averaged over a 3.1 Myr period; Figure 10A). We can see this by comparing the light blue (cyan) circles to the dark blue (navy) circles in Figure 10A. In contrast, for faults active for comparable periods, our studied fault network shows higher lateral propagation rates (i.e., c. 0.38–3.4 mm/year and 0.76–6.9 mm/year based on fault ages of 6.2 and 3.1 Myr respectively), being approximately an order of magnitude faster (compare light green or yellow green circles to red crosses in Figure 10A). However, faults observed over shorter durations (i.e., 105–106 years) appear to have faster

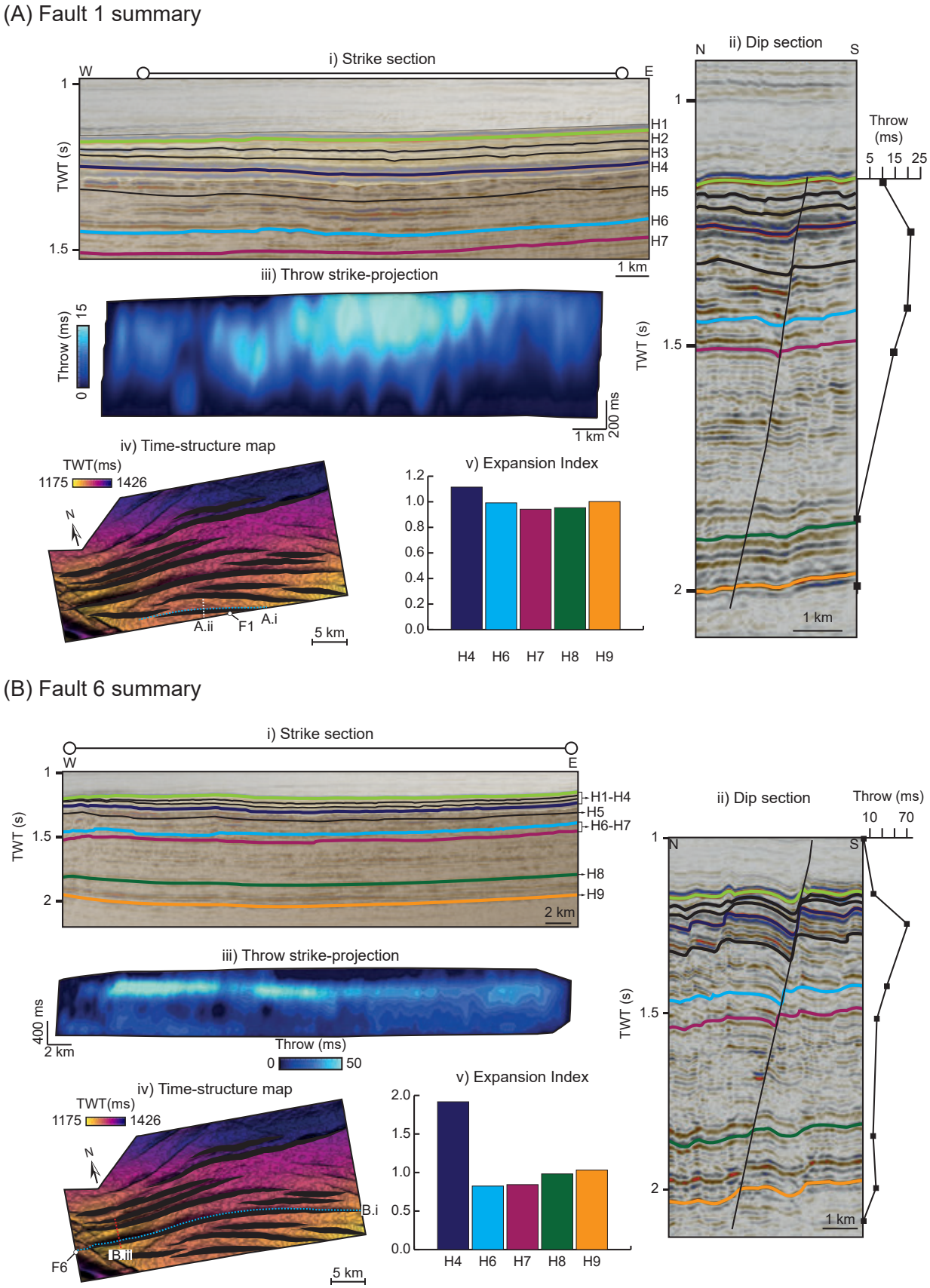

Figure 5 – **(A)** A detailed overview of Fault 1 (F1) showing **(A.i)** a strike-parallel seismic section, **(A.ii)** a strike-perpendicular (dip) seismic section, **(A.iii)** strike-projected throw distribution along the fault surface, **(A.iv)** A time-structure map of the base syn-kinematic horizons (H4) denoting the fault map location and the location of sections (A.i) and (A.ii). **(A.v)** Expansion Index (EI) values showing potential across fault thickening (i.e., syn-kinematic growth) at the H4 level. **(B)** A detailed overview of Fault 6 (F6) showing **(B.i)** a strike-parallel seismic section, **(B.ii)** a strike-perpendicular (dip) seismic section, **(B.iii)** strike-projected throw distribution along the fault surface, **(B.iv)** A time-structure map of the base syn-kinematic horizons (H4) denoting the fault map location and the location of sections (B.i) and (B.ii). **(B.v)** Expansion Index (EI) values showing potential across fault thickening (i.e., syn-kinematic growth) at the H4 level.

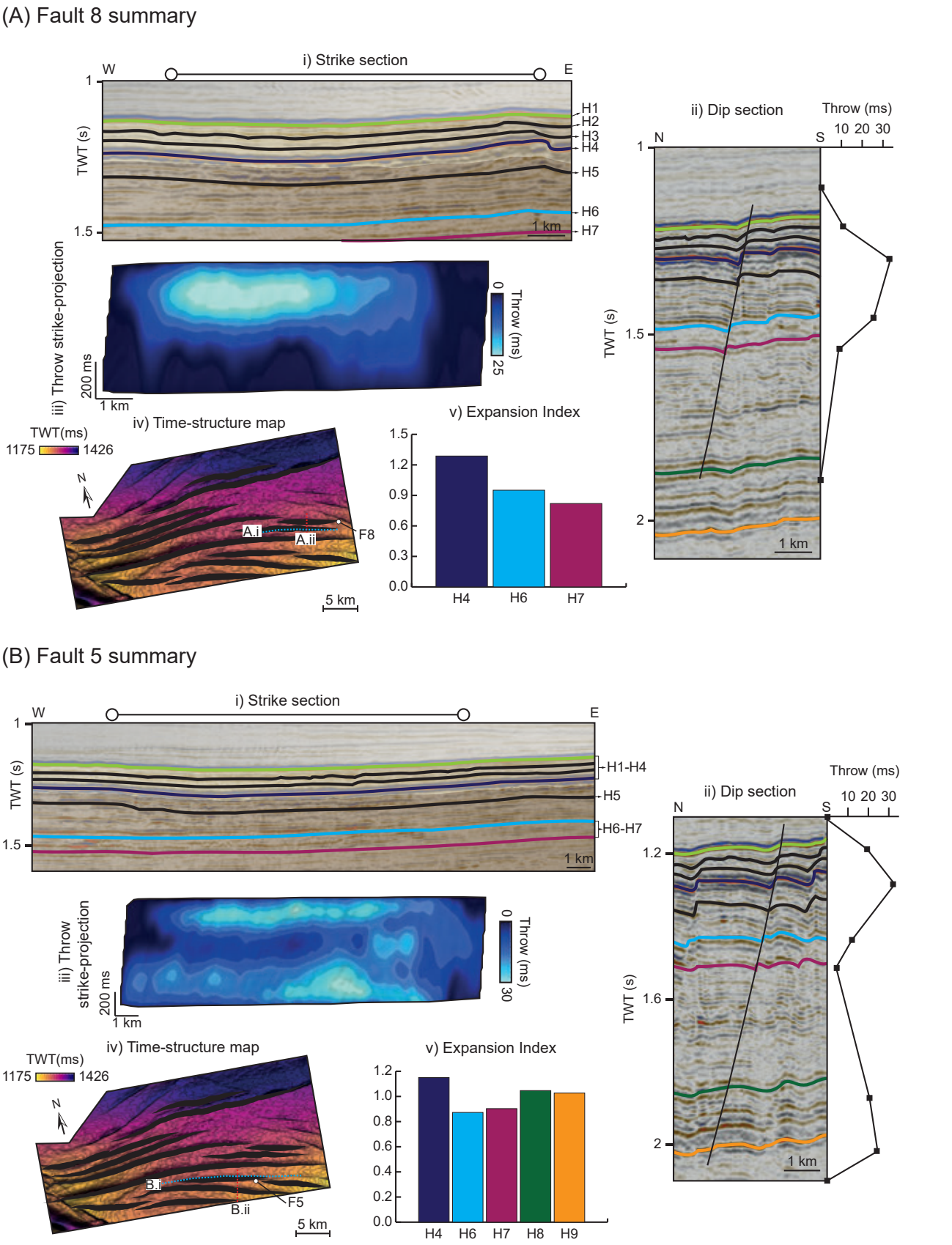

Figure 6 – **(A)** A detailed overview of Fault 8 (F8) showing **(A.i)** a strike-parallel seismic section, **(A.ii)** a strike-perpendicular (dip) seismic section, **(A.iii)** strike-projected throw distribution along the fault surface, **(A.iv)** A time-structure map of the base syn-kinematic horizons (H4) denoting the fault map location and the location of sections (A.i) and (A.ii). **(A.v)** Expansion Index (EI) values showing potential across fault thickening (i.e., syn-kinematic growth) at the H4 level. **(B)** A detailed overview of Fault 5 (F5) showing **(B.i)** a strike-parallel seismic section, **(B.ii)** a strike-perpendicular (dip) seismic section, **(B.iii)** strike-projected throw distribution along the fault surface, **(B.iv)** A time-structure map of the base syn-kinematic horizons (H4) denoting the fault map location and the location of sections (B.i) and (B.ii). **(B.v)** Expansion Index (EI) values showing potential across fault thickening (i.e., syn-kinematic growth) at the H4 level.

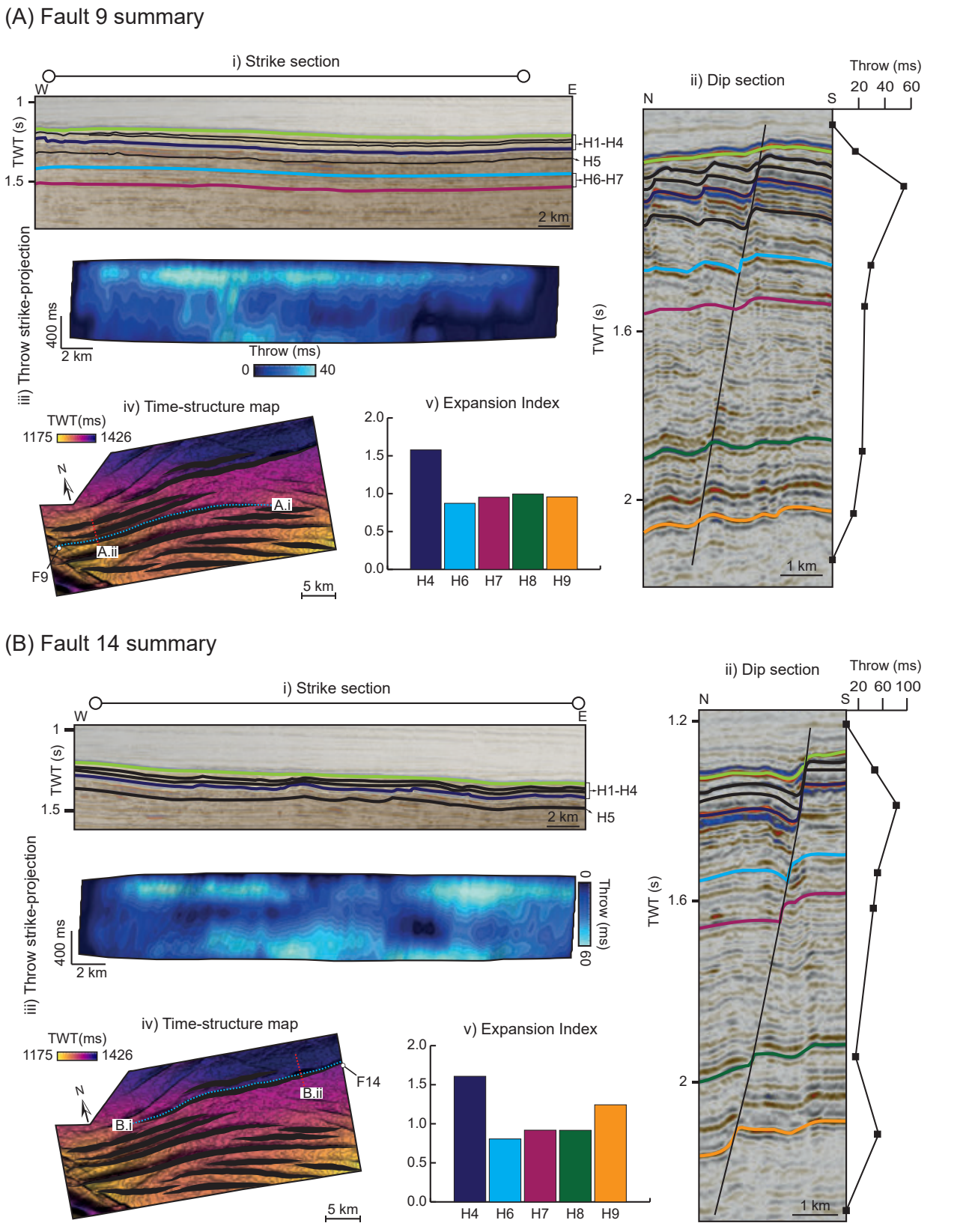

Figure 7 – **(A)** A detailed overview of Fault 8 (F8) showing **(A.i)** a strike-parallel seismic section, **(A.ii)** a strike-perpendicular (dip) seismic section, **(A.iii)** strike-projected throw distribution along the fault surface, **(A.iv)** A time-structure map of the base syn-kinematic horizons (H4) denoting the fault map location and the location of sections (A.i) and (A.ii). **(A.v)** Expansion Index (EI) values showing potential across fault thickening (i.e., syn-kinematic growth) at the H4 level. **(B)** A detailed overview of Fault 550 (F5) showing **(B.i)** a strike-parallel seismic section, **(B.ii)** a strike-perpendicular (dip) seismic section, **(B.iii)** strike-projected throw distribution along the fault surface, **(B.iv)** A time-structure map of the base syn-kinematic horizons (H4) denoting the fault map location and the location of sections (B.i) and (B.ii). **(B.v)** Expansion Index (EI) values showing potential across fault thickening (i.e., syn-kinematic growth) at the H4 level.

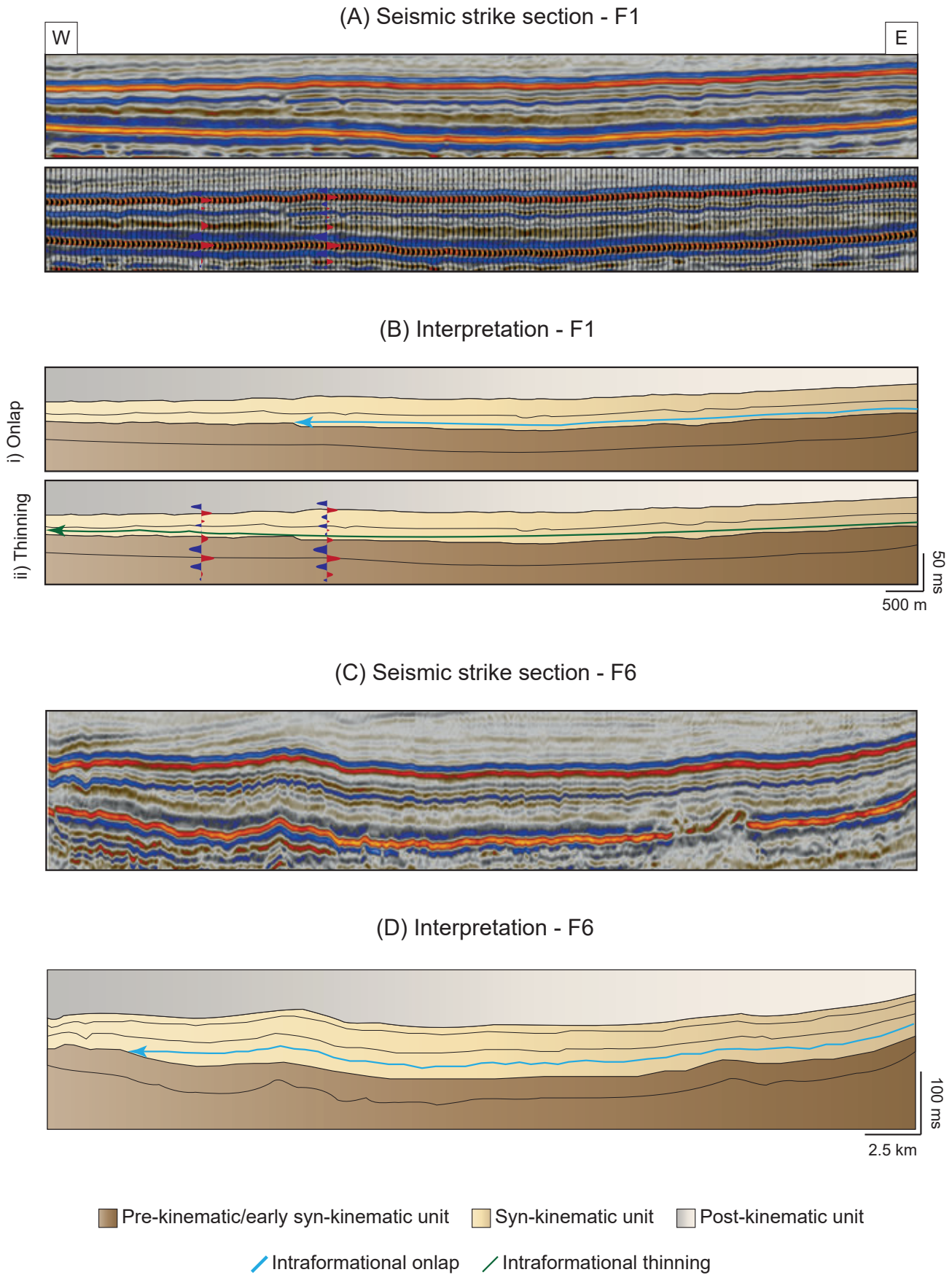

Figure 8 – Un-interpreted and interpreted strike-parallel sections along faults F1 **(A, b)** and F6 **(C, D)** showing the lower-most reflections in Upper Jurassic package onlapping onto the base syn-kinematic horizon immediately adjacent to the fault tips (blue arrow). **(B.i, B.ii)** A schematic representation of two possible interpretations along strike of F1 where the blue arrow shows the onlap and truncation scenario before the fault tip and the green arrow shows the onlap and thinning case towards the fault tip. The two interpretations **(B.i, B.ii)** illustrate the implication of seismic tuning on the observations of the intraformational architecture.

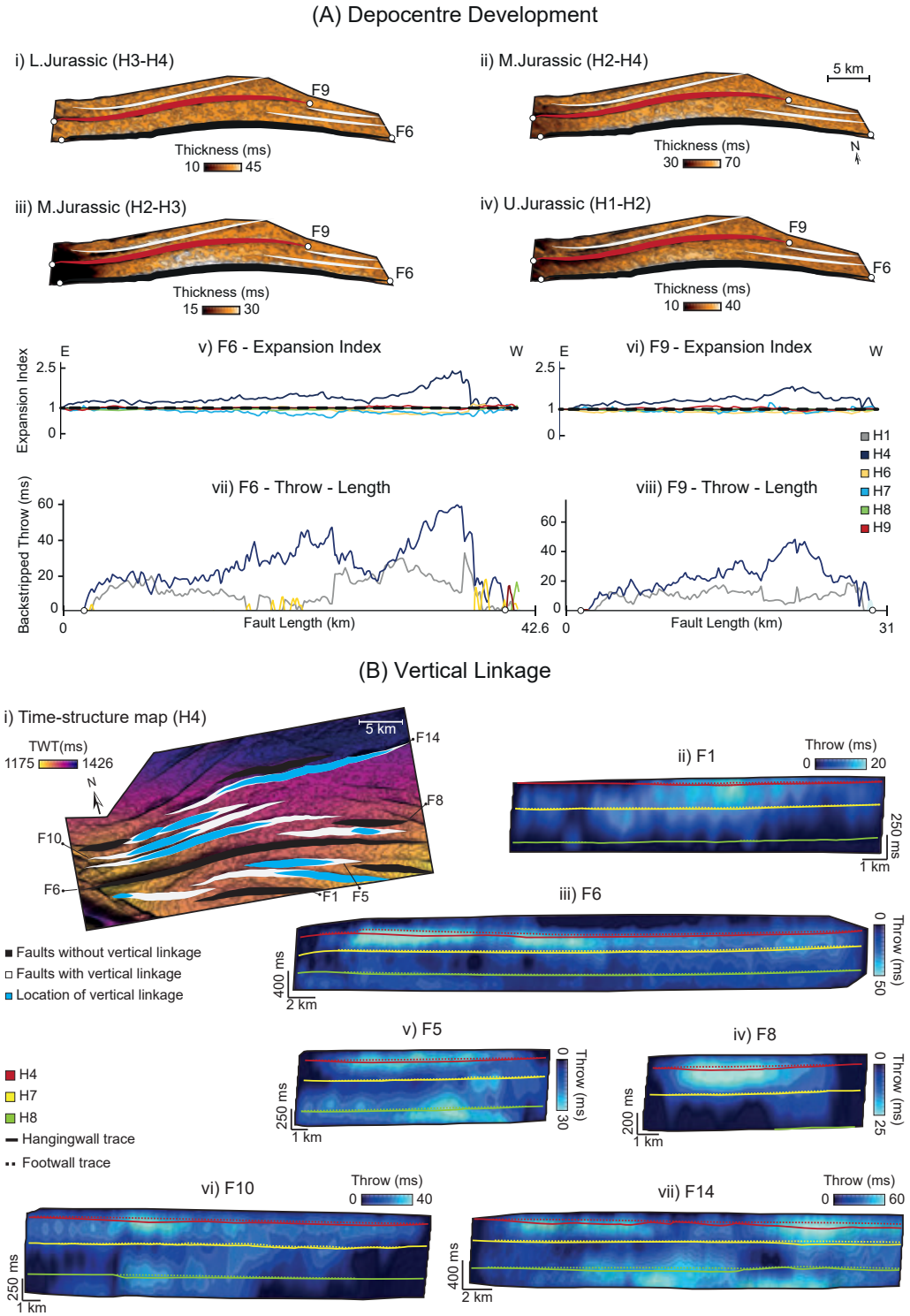

Figure 9 – Un-interpreted and interpreted strike-parallel sections along faults F1 **(A)** A summary of the techniques and results used to understand depocentre development and determine the location of fault tips. **(A.i-iv)** Isochron (time-thickness) maps for sub-units of the syn-kinematic interval (Middle Jurassic to Early Cretaceous) showing across-fault thickening in the smallest resolvable interval. **(A.v)** and **(A.vi)** Expansion Index (EI) values along strike of faults 8 (F6) and 11 (F9) showing values >1 along at the H4 level along strike of the entire fault surface. **(A.vii)** and **(A.viii)** backstripped throw vs. length profiles for F6 and F9 highlighting maximum throw occurring at H4 level and showing the location of the fault tips. **(B)** A description of the variability in vertical linkage across the studied fault network. **(B.i)** Time-structure map of the base syn-kinematic level (H4) showing the studied fault network. Faults coloured in black are the ones that show no sign of vertical linkage while faults coloured in white indicate faults that exhibit vertical linkage. The blue fill-colour within the white faults highlights the map location of the inferred vertical linkage. Strike-projections **(B.ii-vii)** show the fault examples discussed in-text with hangingwall and footwall throw traces indicated by solid and dashed lines for horizons H4, H7, and H8. The strike-projections illustrate the lack of any throw maxima below H7 for subset 1 faults (F1, F6, F8) and the presence of an intraformational detachment layer at H7 that separates different throw maxima above and below the detachment for subset 2 faults (F5, F9, F10).

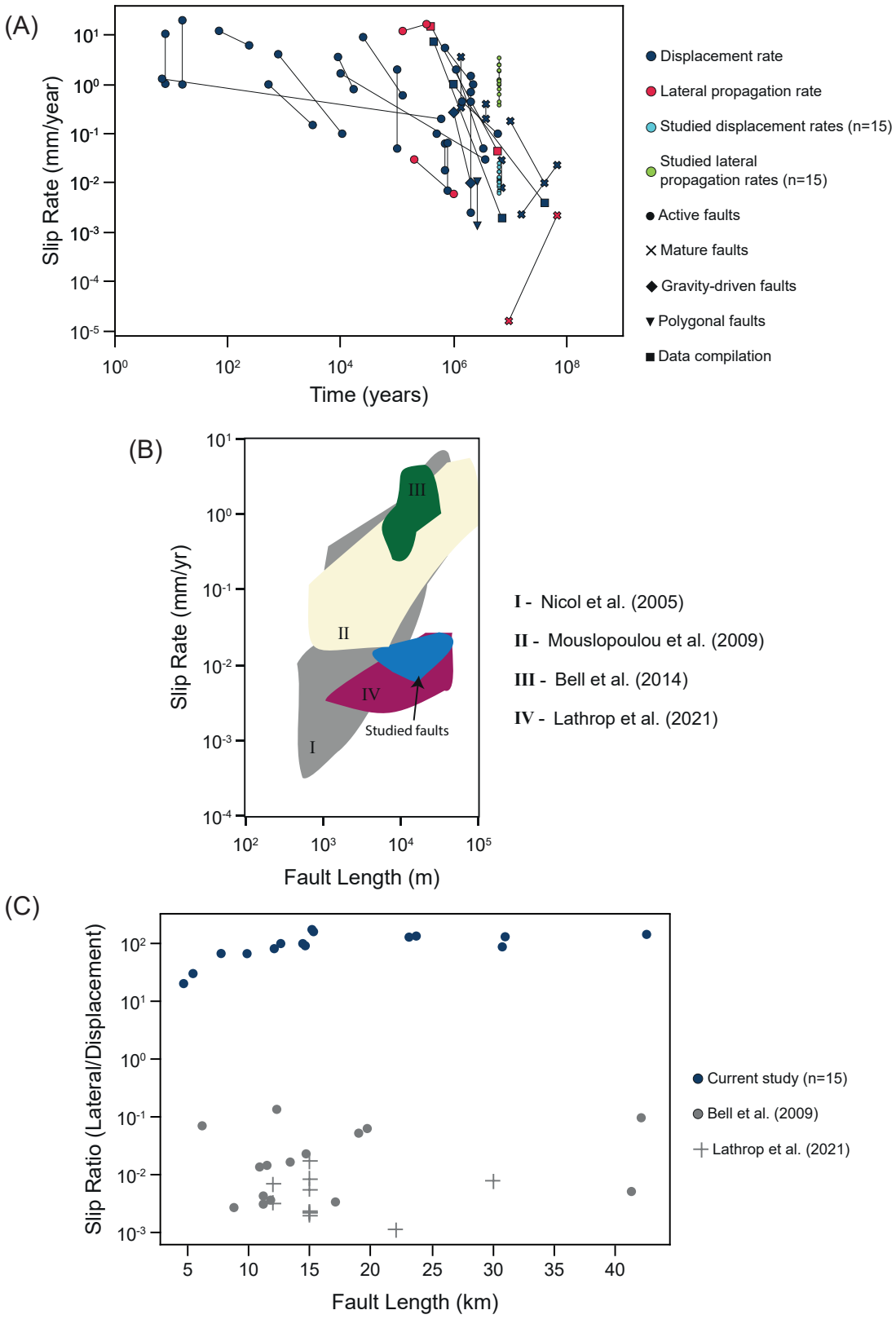

Figure 10 – **(A)** Slip rate data across various timescales for the studied fault network (displacement rates in light blue and lateral propagation rates in light green) and literature data (displacement rates in dark blue and lateral propagation rates in red). The shape of the literature data points relates to their type/origin. Each literature study is represented by two points marking the maximum and minimum reported rates in the study and the line connecting the two points captures the range of reported data by each study. Another version of this plot is provided in Figure SI-2 in Supporting Information where each literature study is clearly indicated, and the literature data is provided in Appendix 2 in *Alghuraybi* (2023). **(B)** Slip rate data (displacement rates) across various fault lengths. **(C)** A plot of the ratio of lateral propagation and displacement rates for the studied faults (dark blue), data from *Bell et al.* (2009) (grey circles) and *Lathrop et al.* (2021) (grey crosses). The plot shows that the studied fault network has a ratio that is 2-3 orders of magnitude higher than other seismically imaged faults of similar length. Please note that we plot the maximum and minimum slip rate data from each study and connect those two points with a line to represent the full range of rates reported (Figure 10A.

lateral propagation rates (i.e., approximately an order to magnitude higher) compared to our studied fault network (compare red circle and square data to light green circles in Fig. 10A).

5 Discussion

Our studied fault network has displacement rates that are comparable to those measured over similar time scales (i.e., >107 years; dark blue crosses compared to light blue circles in Fig. 10A) in the North Sea (*Nicol et al.*, 1997; *Bell et al.*, 2014), the Timor Sea (*Meyer et al.*, 2002), and the Basin & Range and Taranaki Rift (*Mouslopoulou et al.*, 2009), or for faults with similar trace lengths (>104 km; Figure 10B; *Lathrop et al.*, 2021) averaged over longer time scales. However, for faults active for a comparable time period, our studied fault network shows higher lateral propagation rates (i.e., c. 0.38–3.4 mm/year and 0.76–6.9 mm/year based on fault ages of 6.2 and 3.1 Myr respectively), being approximately an order of magnitude faster (compare light green or yellow green circles to red crosses in Figure 10A). Depending on the growth paths these faults took (i.e., constant length model vs. propagating fault model), a relationship should emerge between the rate of lateral propagation, fault displacement rate, and fault maturity. Specifically, if the faults grew in accordance with the propagating fault model, the ratio between lateral propagation and displacement rate will be closer to 1. However, if the faults established their lengths before accruing significant displacement, then the ratio between lateral propagation and displacement would be >1, especially during the early stages of fault development (i.e., initial 20 – 30% of fault lifespan; e.g., *Walsh et al.*, 2002; *Meyer et al.*, 2002; *Nicol et al.*, 2005, 2016; *Childs et al.*, 2017; *Rotevatn et al.*, 2019; *Nicol et al.*, 2020; *Lathrop et al.*, 2022) . We observe that independent of fault length and whether the duration of faulting is estimated to be 6.2 or 3.1 Myr, the studied faults propagated laterally much more rapidly (i.e., c. 300–20 times faster) than they accumulated displacement (Figure 10C). This value is 2-3 orders of magnitude higher than for other seismically imaged faults of similar length (Figure 10C; e.g., *Bell et al.*, 2009; *Lathrop et al.*, 2021).

The studied fault network is characterised by faults having i) low (c. 0.001) D_{max}/L_{max} scaling relationships (Figure 4A), ii) high (>5) length/height aspect ratios (Figure 4B), iii) a broad, bell-shaped throw-length profile at the base syn-kinematic level (H4; Figure 4C), iv) hangingwall depocenters forming at first detectable unit above the base syn-kinematic horizon (H4; Figure 4A), and v) onlap of the lowermost syn-kinematic strata onto pre-kinematic strata immediately inboard of the lateral fault tips (Fig. 8). The thinning and onlapping of earliest syn-rift sediments immediately adjacent to the lateral tips of the normal faults we describe here (Figure 8A, B) is also observed in other large normal faults in the Gulf of Suez, Egypt (see Figure 3A in *Gawthorpe et al.*, 2003) and the East African Rift (*Morley*, 1999), where this stratigraphic architecture is interpreted to reflect early establishment of the near-final fault length, consistent with the constant-length model. In contrast, if the faults grew by simultaneously accumulating length and displacement (i.e., 'propagating fault model'), then we would expect to observe progressive onlapping of the syn-kinematic strata towards the lateral tips of the faults (*Morley*, 1999, see Figure 2 in). These geometric observations suggest that the studied network captures faults during their very earliest stage of development when they were growing in accordance with the constant-length model (Figure 11). We do not think that these faults are atypical for tectonic normal faults in terms of their general structure and evolution. However, they are unusual in the sense that they: (i) became inactive relatively early in their histories, prior to accumulating significant displacement (see *Walsh et al.*, 2002); and (ii) they are imaged in a high-quality, 3D seismic reflection dataset. Some of the studied faults are tip-restricted (e.g., F2, F6, F8, F9, F10, F13) as indicted by faults having higher throw gradients near their branchpoints (and presumably branchlines; e.g., *Nicol et al.*, 1996). This means that the tip-restricted faults would likely have propagated further and thus have been longer in the absence of the oblique faults, meaning our reported lengths are conservative estimates. Nevertheless, this does not detract from our conclusion, given these faults are already long for their displacement and if not tip-restricted would presumably have grown even longer.

Along with the geometric properties of the fault network, our kinematic analysis shows that these faults propagated laterally much faster than they accumulated displacement (Figures 10C, 11). Combining the geometric and kinematic observations indicates that the studied faults rapidly lengthened and reached their near-final lengths but did not have a chance to accumulate significant additional displacement (i.e., faults are geometrically immature) before becoming inactive (e.g., *Walsh et al.*, 2002; *Meyer et al.*, 2002; *Nicol et al.*, 2005, 2016; *Childs et al.*, 2017). Why the faults became inactive is unknown, although we suspect this is related to strain localisation on to the nearby, very large (c. 2 km displacement), basement-rooted, Troms-Finnmark Fault Complex (TFFC), which continued to be active until the Eocene (e.g., *Alghuraybi et al.*, 2022). It could be argued that the presence of a weak mudstone at the bottom of the faulted interval inhibits downward propagation and limits the accumulation of additional displacement, leading to high aspect ratios (*Schultz and Fossen*, 2002). However, we show that observations from subset 2 faults (i.e., multiple throw maxima along different stratigraphic intervals separated by a throw minimum) indicates the presence of an intraformational detachment layer, where subset 2 faults likely nucleated at different stratigraphic levels (H4, H9) and vertically linked at a later stage during the faults' lives (Figure 9B *Nicol et al.*, 1996; *Soliva and Benedicto*, 2005;

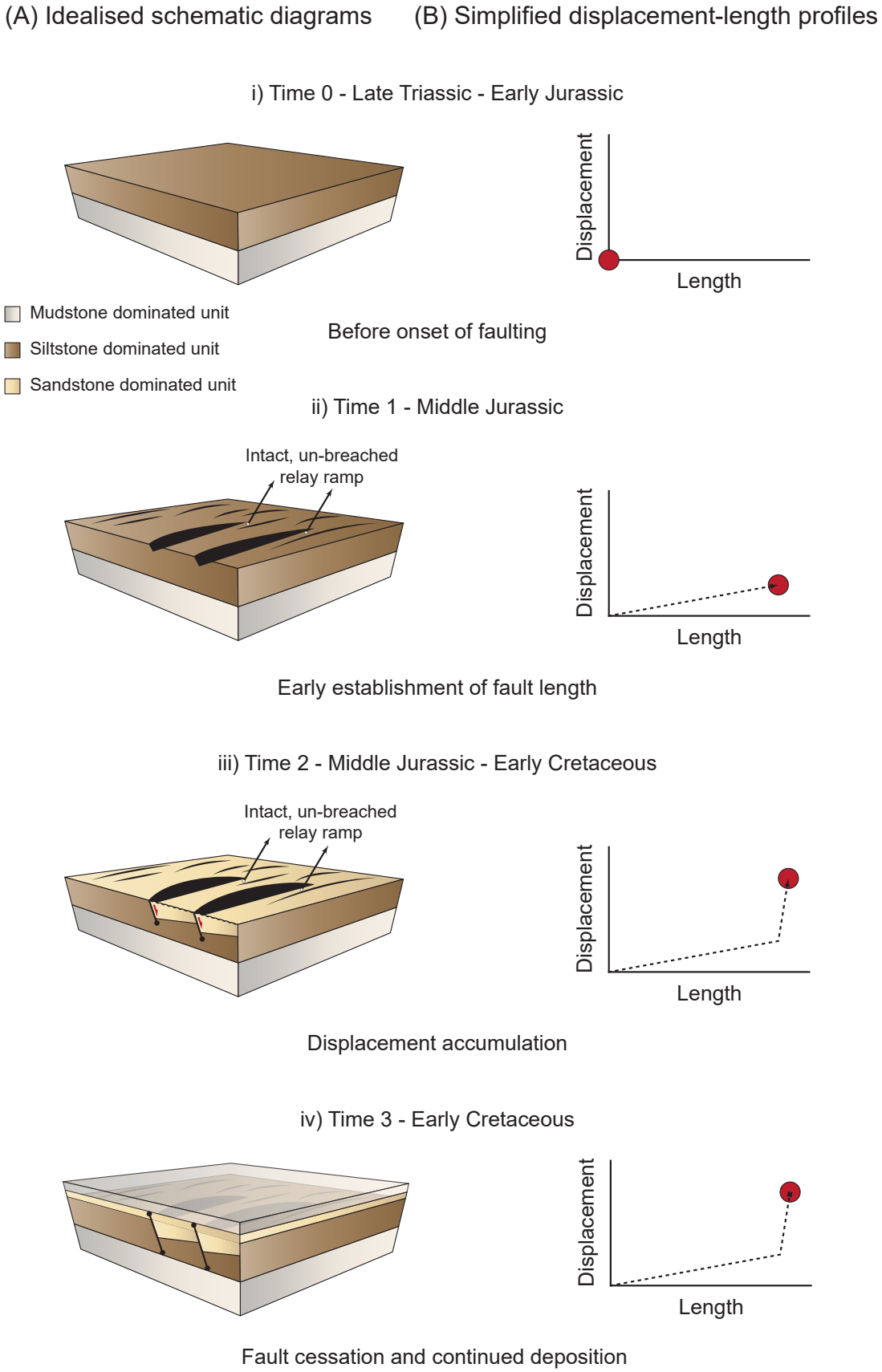

Figure 11 – **(A)** Idealised schematic diagrams summarising our proposed structural evolution for the studied fault network. These schematic diagrams cover the time steps before the onset of faulting **(A.i)** to the fault cessation and continued deposition time step **(A.iv)**. The geological ages represent the studied fault network but for a more theoretical and generalised model, these time steps can be viewed as time 0 (oldest) to time 3 (youngest). **(B)** a simplified graphical representation of our fault growth model in the displacement-length domain. These plots show the rapid lateral propagation rate (early establishment of fault length **(B.i-ii)** and the subsequent displacement accumulation **(B.iii)** before growth arrest **(B.iv)**.

Roche et al., 2013, 2021). Therefore, we maintain that the early formation of strike-parallel hangingwall depocenters (Figure 9A) and the observed onlap relationships (Figure 8), combined with the other geometric properties of the fault network, favour the interpretation of the rapid propagation rate being a function of early-stage faulting rather than vertical restriction alone.

The highest aspect ratio ever reported for a natural normal fault that we are aware of is 14 (*Nicol et al.*, 1996; *Soliva and Benedicto*, 2005; *Roche et al.*, 2013, 2021); this is significantly lower than the highest aspect ratio we observe here (c. 25). In fact, six of the studied faults have aspect ratios »14 (Figure 4B). Numerical models, motivated by observations from meter-scale fault networks in layered carbonate rocks, show that aspect ratios can vary through time, increasing when the faults interact with layers that restrict their onwards vertical propagation, before decreasing again when they are able to breach those layers (e.g., *Soliva and Benedicto*, 2005; *Roche et al.*, 2013). Our study suggests that this process may occur at substantially larger scales than previously reported, meaning aspect ratio variability is a fundamental aspect of fault growth across scales in mechanically layered rocks. The variability in the geometric and kinematic properties of the studied fault network might be explained by the variable and complex vertical growth history of individual structures, which likely reflects the role of the marked lithological and likely strong mechanical anisotropy observed in wellbore data (Figure 1C).

Our slip rate data compilation builds on previous works (e.g., *Nicol et al.*, 2005; *Mouslopoulou et al.*, 2009; *Nicol et al.*, 2020) and includes lateral propagation and displacement rate data measured over a range of temporal scales using different methods (geodetic, GPS, field observations, seismic refraction, and reflection data). By compiling the database, we note that lateral propagation rates are often not reported or less frequently documented compared to displacement rates. Based on this, we propose to document, where possible, both displacement and lateral propagation rates. By doing so, we can further our understanding of how faults evolve across various temporal and spatial scales.

6 Conclusion

We study a normal fault network from the SW Barents Sea, offshore Norway using high-quality 3D seismic reflection and borehole data. The fault network consists of 15 Middle Jurassic to Early Cretaceous normal faults that offset a Late Triassic to Early Cretaceous stratigraphy and are associated with Upper Jurassic growth strata. These faults are characterised by i) anomalously low (c. 0.001) D_{max}/L_{max} scaling relationships, ii) unusually high (up to 25) aspect ratios, iii) broad, bell-shaped throw-length profile at the base syn-kinematic level, and iv) hangingwall depocenters forming within the first detectable unit above the base syn-kinematic horizon. By quantifying the faults' lateral propagation (c. 0.76–6.9 mm/year) and displacement accumulation (c. 0.012–0.050 mm/year) rates, we show that these faults developed up to 300 times faster than accumulated displacement. Based on the geometric properties of these faults and their rapid lateral propagation relative to displacement accumulation rates, we propose that these faults represent a "fossilised" snapshot of the earliest stages of normal fault growth, where the faults reached their near-final lengths before accumulating any significant displacement resulting in geometrically immature faults.

Acknowledgements

The results presented here are part of A. Alghuraybi's PhD research at Imperial College London, funded by Saudi Aramco. We thank the Norwegian Petroleum Directorate for the publicly available data (https://-portal.diskos.cgg.com/whereoil-data/) and Schlumberger for Petrel software. We also thank the reviewers Lisa McNeill and Vincent Roche, the Handling editor Frank Zwaan and Executive editor Gwen Peron-Pinvidic for their constructive feedback and helpful suggestions that helped improve this work. We would like to express our gratitude to the Landscapes and Basins Research group at Imperial College London, specifically Amir Joffe and Mahmoud ElYamani, for their valuable contributions and insightful discussions during the various stages of preparing this work. We thank Andy Nicol and William Clyde for the constructive feedback on a previous version of this work.

Author contributions

AA: data analysis, investigation, conceptualisation, writing – original draft; **RB**: conceptualisation, supervision, writing – review and editing; **CJ**: conceptualisation, supervision, writing – review and editing

Data availability

The seismic and wellbore data are openly available in the Norwegian national data repository for petroleum data at https://portal.diskos.cgg.com/whereoil-data/. Detailed geometric analysis of all 15 studied faults is provided in Figure SI-3, in Supporting Information. The depth conversion data (Appendix 1) and slip rate data compilation (Appendix 2) are available at https://-doi.org/10.6084/m9.figshare.21681107.v4.

Competing interests

The authors declare no competing interests.

Peer review

This publication was peer-reviewed by Lisa McNeill and Vincent Roche. The full peer-review report can be found here: https://tektonika.online/index.php/home/article/view/29/27

Copyright notice

References

Alghuraybi, A. (2023), Slip rate data compilation and depth conversion data, doi: 10.6084/m9.figshare.21681107.v4.

Alghuraybi, A., R. E. Bell, and C. A. Jackson (2022), The geometric and temporal evolution of fault-related folds constrain normal fault growth patterns, Barents Sea, offshore Norway, *Basin Research*, *34*(2), 618–639, doi: 10.1111/bre.12633.

Bakke, K., I. A. Kane, O. J. Martinsen, S. A. Petersen, T. A. Johansen, S. Hustoft, F. H. Jacobsen, and A. Groth (2013), Seismic modeling in the analysis of deep-water sandstone termination styles, *AAPG Bulletin*, *97*(9), 1395–1419, doi: 10.1306/03041312069.

Bell, R. E., L. C. McNeill, J. M. Bull, T. J. Henstock, R. E. L. Collier, and M. R. Leeder (2009), Fault architecture, basin structure and evolution of the Gulf of Corinth Rift, central Greece, *Basin Research*, *21*(6), 824–855, doi: 10.1111/j.1365-2117.2009.00401.x.

Bell, R. E., C. A. Jackson, P. S. Whipp, and B. Clements (2014), Strain migration during multiphase extension: Observations from the northern North Sea, *Tectonics*, *33*(10), 1936–1963, doi: 10.1002/2014TC003551.

Blakeslee, M. W., and S. A. Kattenhorn (2013), Revised earthquake hazard of the Hat Creek fault, northern California: A case example of a normal fault dissecting variable-age basaltic lavas, *Geosphere*, *9*(5), 1397–1409, doi: 10.1130/GES00910.1.

Briole, P., A. Rigo, H. Lyon-Caen, J. C. Ruegg, K. Papazissi, C. Mitsakaki, A. Balodimou, G. Veis, D. Hatzfeld, and A. Deschamps (2000), Active deformation of the Corinth rift, Greece: Results from repeated Global Positioning System surveys between 1990 and 1995, *Journal of Geophysical Research, [Solid Earth]*, *105*(B11), 25,605–25,625, doi: 10.1029/2000JB900148.

Brown, A. R. (2001), Color in seismic display, *Leading Edge*, *20*(5), 549–549, doi: 10.1190/1.1438992.

Bull, J. M., T. A. Minshull, N. C. Mitchell, K. Thors, J. K. Dix, and A. I. Best (2003), Fault and magmatic interaction within Iceland's western rift over the last 9 kyr, *Geophysical Journal International*, *154*(1), F1–F8, doi: 10.1046/j.1365-246X.2003.01990.x.

Cartwright, J., R. Bouroullec, D. James, and H. Johnson (1998), Polycyclic motion history of some Gulf Coast growth faults from high-resolution displacement analysis, *Geology*, *26*(9), 819, doi: 10.1130/0091-7613(1998)026<0819:PMHOSG>2.3.CO;2.

Cartwright, J. A., B. D. Trudgill, and C. S. Mansfield (1995), Fault growth by segment linkage: an explanation for scatter in maximum displacement and trace length data from the Canyonlands Grabens of SE Utah, *Journal of Structural Geology*, *17*(9), 1319–1326, doi: 10.1016/0191-8141(95)00033-A.

Childs, C., A. Nicol, J. J. Walsh, and J. Watterson (2003), The growth and propagation of synsedimentary faults, *Journal of Structural Geology*, *25*(4), 633–648, doi: 10.1016/S0191-8141(02)00054-8.

Childs, C., R. E. Holdsworth, C. A. Jackson, T. Manzocchi, J. J. Walsh, and G. Yielding (2017), Introduction to the geometry and growth of normal faults, *Geological Society, London, Special Publications*, *439*(1), 1–9, doi: 10.1144/SP439.24.

Clark, S. A., J. I. Faleide, J. Hauser, O. Ritzmann, R. Mjelde, J. Ebbing, H. Thybo, and E. Flüh (2013), Stochastic velocity inversion of seismic reflection/refraction traveltime data for rift structure of the southwest Barents Sea, *Tectonophysics*, *593*, 135–150, doi: 10.1016/j.tecto.2013.02.033.

Corredor, F., J. H. Shaw, and F. Bilotti (2005), Structural styles in the deep-water fold and thrust belts of the Niger Delta, *AAPG Bulletin*, *89*(6), 753–780, doi: 10.1306/02170504074.

Cowie, P. A., and C. H. Scholz (1992), Displacement-length scaling relationship for faults: data synthesis and discussion, *Journal of Structural Geology*, *14*(10), 1149–1156, doi: 10.1016/0191-8141(92)90066-6.

Cowie, P. A., C. Vanneste, and D. Sornette (1993), Statistical physics model for the spatiotemporal evolution of faults, *Journal of Geophysical Research, [Solid Earth]*, *98*(B12), 21,809–21,821, doi: 10.1029/93JB02223.

Cowie, P. A., G. P. Roberts, J. M. Bull, and F. Visini (2012), Relationships between fault geometry, slip rate variability and earthquake recurrence in extensional settings: Fault geometry control on earthquake rupture, *Geophysical Journal International*, *189*(1), 143–160, doi: 10.1111/j.1365-246X.2012.05378.x.

Doré, A. G. (1995), Barents Sea Geology, Petroleum Resources and Commercial Potential, *Arctic*, *48*(3), 207–221.

Faleide, J. I., F. Tsikalas, A. J. Breivik, R. Mjelde, O. Ritzmann, Ø. Engen, J. Wilson, and O. Eldholm (2008), Structure and evolution of the continental margin off Norway and the Barents Sea, *Episodes*, *31*(1), 82–91, doi: 10.18814/epiiugs/2008/v31i1/012.

Friedrich, A. M., B. P. Wernicke, N. A. Niemi, R. A. Bennett, and J. L. Davis (2003), Comparison of geodetic and geologic data from the Wasatch region, Utah, and implications for the spectral character of Earth deformation at periods of 10 to 10 million years: COMPARISON OF GEODETIC AND GEOLOGIC DATA IN UTAH, *Journal of Geophysical Research, [Solid Earth]*, *108*(B4), doi: 10.1029/2001JB000682.

Gawthorpe, R. L., I. Sharp, J. R. Underhill, and S. Gupta (1997), Linked sequence stratigraphic and structural evolution of propagating normal faults, *Geology*, *25*(9), 795, doi: 10.1130/0091-7613(1997)025<0795:LSSASE>2.3.CO;2.

Gawthorpe, R. L., C. A. Jackson, M. J. Young, I. R. Sharp, A. R. Moustafa, and C. W. Leppard (2003), Normal fault growth, displacement localisation and the evolution of normal fault populations: the Hammam Faraun fault block, Suez rift, Egypt, *Journal of Structural Geology*, *25*(6), 883–895, doi: 10.1016/S0191-8141(02)00088-3.

Gillespie, P. A., J. J. Walsh, and J. Watterson (1992), Limitations of dimension and displacement data from single faults and the consequences for data analysis and interpretation, *Journal of Structural Geology*, *14*(10), 1157–1172, doi: 10.1016/0191-8141(92)90067-7.

Jackson, C. A., and A. Rotevatn (2013), 3D seismic analysis of the structure and evolution of a salt-influenced normal fault zone: A test of competing fault growth models, *Journal of Structural Geology*, *54*, 215–234, doi: 10.1016/j.jsg.2013.06.012.

Jackson, C. A., R. E. Bell, A. Rotevatn, and A. B. M. Tvedt (2017), Techniques to determine the kinematics of synsedimentary normal faults and implications for fault growth models, *Geological Society, London, Special Publications*, *439*(1), 187–217, doi: 10.1144/SP439.22.

Jackson, J., R. Norris, and J. Youngson (1996), The structural evolution of active fault and fold systems in central Otago, New Zealand: evidence revealed by drainage patterns, *Journal of Structural Geology*, *18*(2-3), 217–234, doi: 10.1016/S0191-8141(96)80046-0.

Kim, Y.-S., and D. J. Sanderson (2005), The relationship between displacement and length of faults: a review, *Earth-Science Reviews*, *68*(3-4), 317–334, doi: 10.1016/j.earscirev.2004.06.003.

Lathrop, B. A., C. C. A. Jackson, R. E. Bell, and A. Rotevatn (2021), Normal Fault Kinematics and the Role of Lateral Tip Retreat: An Example From Offshore NW Australia, *Tectonics*, *40*(5), doi: 10.1029/2020TC006631.

Lathrop, B. A., C. A. Jackson, R. E. Bell, and A. Rotevatn (2022), Displacement/Length Scaling Relationships for Normal Faults; a Review, Critique, and Revised Compilation, *Frontiers of Earth Science in China*, *10*, 907,543, doi: 10.3389/feart.2022.907543.

Manighetti, I., M. Campillo, S. Bouley, and F. Cotton (2007), Earthquake scaling, fault segmentation, and structural maturity, *Earth and planetary science letters*, *253*(3-4), 429–438, doi: 10.1016/j.epsl.2006.11.004.

Meyer, V., A. Nicol, C. Childs, J. J. Walsh, and J. Watterson (2002), Progressive localisation of strain during the evolution of a normal fault population, *Journal of Structural Geology*, *24*(8), 1215–1231, doi: 10.1016/S0191-8141(01)00104-3.

Morewood, N. C., and G. P. Roberts (1999), Lateral propagation of the surface trace of the South Alkyonides normal fault segment, central Greece: its impact on models of fault growth and displacement–length relationships, *Journal of Structural Geology*, *21*(6), 635–652, doi: 10.1016/S0191-8141(99)00049-8.

Morley, C. K. (1999), Patterns of displacement along large normal faults: Implications for basin evolution and fault propagation, based on examples from east africa, *AAPG bulletin*, *83 (1999)*, doi: 10.1306/00aa9c0a-1730-11d7-8645000102c1865d.

Mouslopoulou, V., J. J. Walsh, and A. Nicol (2009), Fault displacement rates on a range of timescales, *Earth and planetary science letters*, *278*(3-4), 186–197, doi: 10.1016/j.epsl.2008.11.031.

Mouslopoulou, V., A. Nicol, J. J. Walsh, J. G. Begg, D. B. Townsend, and D. T. Hristopulos (2012), Fault-slip accumulation in an active rift over thousands to millions of years and the importance of paleoearthquake sampling, *Journal of Structural Geology*, *36*, 71–80, doi: 10.1016/j.jsg.2011.11.010.

Nicol, A., J. Watterson, J. J. Walsh, and C. Childs (1996), The shapes, major axis orientations and displacement patterns of fault surfaces, *Journal of Structural Geology*, *18*(2-3), 235–248, doi: 10.1016/S0191-8141(96)80047-2.

Nicol, A., J. J. Walsh, J. Watterson, and J. R. Underhill (1997), Displacement rates of normal faults, *Nature*, *390*(6656), 157–159, doi: 10.1038/36548.

Nicol, A., J. J. Walsh, T. Manzocchi, and N. Morewood (2005), Displacement rates and average earthquake recurrence intervals on normal faults, *Journal of Structural Geology*, *27*(3), 541–551, doi: 10.1016/j.jsg.2004.10.009.

Nicol, A., J. J. Walsh, P. Villamor, H. Seebeck, and K. R. Berryman (2010), Normal fault interactions, paleoearthquakes and growth in an active rift, *Journal of Structural Geology*, *32*(8), 1101–1113, doi: 10.1016/j.jsg.2010.06.018.

Nicol, A., R. Robinson, R. Van Dissen, and A. Harvison (2016), Variability of recurrence interval and single-event slip for surface-rupturing earthquakes in New Zealand, *New Zealand Journal of Geology and Geophysics*, *59*(1), 97–116, doi: 10.1080/00288306.2015.1127822.

Nicol, A., V. Mouslopoulou, J. Begg, and O. Oncken (2020), Displacement Accumulation and Sampling of Paleoearthquakes on Active Normal Faults of Crete in the Eastern Mediterranean, *Geochemistry, Geophysics, Geosystems*, *21*(11), doi: 10.1029/2020GC009265.

NPD (2023), Wellbore: 7124/4-1 S, *Tech. Rep. 7124/4-1 S*, Norwegian Petroleum Directorate.

Osagiede, E. E., O. B. Duffy, C. A. Jackson, and T. Wrona (2014), Quantifying the growth history of seismically imaged normal faults, *Journal of Structural Geology*, *66*, 382–399, doi: 10.1016/j.jsg.2014.05.021.

Robinson, R., A. Nicol, J. J. Walsh, and P. Villamor (2009), Features of earthquake occurrence in a complex normal fault network: Results from a synthetic seismicity model of the Taupo Rift, New Zealand, *Journal of geophysical research*, *114*(B12), B12,306, doi: 10.1029/2008JB006231.

Robson, A. G., R. C. King, and S. P. Holford (2017), Structural evolution of a gravitationally detached normal fault array: analysis of 3D seismic data from the Ceduna Sub-Basin, Great Australian Bight, *Basin Research*, *29*(5), 605–624, doi: 10.1111/bre.12191.

Roche, V., C. Homberg, and M. Rocher (2013), Fault nucleation, restriction, and aspect ratio in layered sections: Quantification of the strength and stiffness roles using numerical modeling: FAULT MODELING IN LAYERED SECTIONS, *Journal of Geophysical Research, [Solid Earth]*, *118*(8), 4446–4460, doi: 10.1002/jgrb.50279.

Roche, V., G. Camanni, C. Childs, T. Manzocchi, J. Walsh, J. Conneally, M. M. Saqab, and E. Delogkos (2021), Variability in the three-dimensional geometry of segmented normal fault surfaces, *Earth-Science Reviews*, *216*, 103,523, doi: 10.1016/j.earscirev.2021.103523.

Rojo, L. A., N. Cardozo, A. Escalona, and H. Koyi (2019), Structural style and evolution of the Nordkapp Basin, Norwegian Barents Sea, *AAPG Bulletin*, *103*(9), 2177–2217, doi: 10.1306/01301918028.

Rotevatn, A., C. A. Jackson, A. B. M. Tvedt, R. E. Bell, and I. Blækkan (2019), How do normal faults grow?, *Journal of Structural Geology*, *125*, 174–184, doi: 10.1016/j.jsg.2018.08.005.

Schlische, R. W., S. S. Young, R. V. Ackermann, and A. Gupta (1996), Geometry and scaling relations of a population of very small rift-related normal faults, *Geology*, *24*(8), 683–686, doi: 10.1130/0091-7613(1996)024<0683:GASROA>2.3.CO;2.

Scholz, C. A., T. C. Moore, D. R. Hutchinson, A. J. Golmshtok, K. D. Klitgord, and A. G. Kurotchkin (1998), Comparative sequence stratigraphy of low-latitude versus high-latitude lacustrine rift basins: seismic data examples from the East African and Baikal rifts, *Palaeogeography, palaeoclimatology, palaeoecology*, *140*(1-4), 401–420, doi: 10.1016/S0031-0182(98)00022-4.

Schultz, R. A., and H. Fossen (2002), Displacement–length scaling in three dimensions: the importance of aspect ratio and application to deformation bands, *Journal of Structural Geology*, *24*(9), 1389–1411, doi: 10.1016/S0191-8141(01)00146-8.

Shillington, D. J., C. A. Scholz, P. R. N. Chindandali, J. B. Gaherty, N. J. Accardo, E. Onyango, C. J. Ebinger, and A. A. Nyblade (2020), Controls on Rift Faulting in the North Basin of the Malawi (Nyasa) Rift, East Africa, *Tectonics*, *39*(3), doi: 10.1029/2019TC005633.

Soliva, R., and A. Benedicto (2005), Geometry, scaling relations and spacing of vertically restricted normal faults, *Journal of Structural Geology*, *27*(2), 317–325, doi: 10.1016/j.jsg.2004.08.010.

Spathopoulos, F. (1996), An insight on salt tectonics in the Angola Basin, South Atlantic, *Geological Society, London, Special Publications*, *100*(1), 153–174, doi: 10.1144/GSL.SP.1996.100.01.11.

Wallace, L. M., S. Ellis, T. Little, P. Tregoning, N. Palmer, R. Rosa, R. Stanaway, J. Oa, E. Nidkombu, and J. Kwazi (2014), Continental breakup and UHP rock exhumation in action: GPS results from the Woodlark Rift, Papua New Guinea, *Geochemistry, Geophysics, Geosystems*, *15*(11), 4267–4290, doi: 10.1002/2014GC005458.

Walsh, J. J., and J. Watterson (1988), Analysis of the relationship between displacements and dimensions of faults, *Journal of Structural Geology*, *10*(3), 239–247, doi: 10.1016/0191-8141(88)90057-0.

Walsh, J. J., and J. Watterson (1991), Geometric and kinematic coherence and scale effects in normal fault systems, *Geological Society, London, Special Publications*, *56*(1), 193–203, doi: 10.1144/GSL.SP.1991.056.01.13.

Walsh, J. J., A. Nicol, and C. Childs (2002), An alternative model for the growth of faults, *Journal of Structural Geology*, *24*(11), 1669–1675, doi: 10.1016/S0191-8141(01)00165-1.

Walsh, J. J., W. R. Bailey, C. Childs, A. Nicol, and C. G. Bonson (2003), Formation of segmented normal faults: a 3-D perspective, *Journal of Structural Geology*, *25*(8), 1251–1262, doi: 10.1016/S0191-8141(02)00161-X.

Watterson, J. (1986), Fault dimensions, displacements and growth, *Pure and Applied Geophysics PAGEOPH*, *124*(1-2), 365–373, doi: 10.1007/BF00875732.